



Spectroscopic Characterisation of New Accreting Intermediate-Mass Pre-Main Sequence Stars

Shima Ujjani Shivashankara

Submitted in accordance with the requirements for the degree of
Master of Science by Research

The University of Leeds
School of Physics and Astronomy

November 2019

The candidate confirms that the work submitted is her own and that appropriate credit has been given where reference has been made to the work of others.

This copy has been supplied on the understanding that it is copyright material and that no quotation from the thesis may be published without proper acknowledgment.

The right of Shima Ujjani Shivashankara to be identified as Author of this work has been asserted by Shima Ujjani Shivashankara in accordance with the Copyright, Designs and Patents Act 1988.

Acknowledgements

I am extremely grateful to Olja Panić, my supervisor, and thank you for your expert guidance and more importantly for keeping me motivated throughout. To my co-supervisor, René Oudmaijer thank you for your constant support, patience and knowledge you shared with me.

I would like to extend my thanks to my fellow students in the Leeds Astrophysics group for creating a friendly environment. In particular, thanks to James Miley and Miguel Vioque for the useful discussions. I thank Chumpon Wichittanakom who has greatly helped in my studies.

Important special thanks to my parents for always being there for me, motivating me and supporting me, both emotionally and financially. Without your love and encouragement I wouldn't reach this far.

Thank you.

Abstract

The thesis presents the spectroscopic study of the stellar parameters, accretion rates and IR excess of Herbig Ae/Be stars. The discs around solar mass stars are expected to evolve differently compared to those around intermediate-mass stars because the stars evolve differently. However, more complete samples of young pre-main sequence stars are not present in literature to quantify the differences. Most current studies in the stellar range of intermediate-mass focuses on the Herbig Ae population, a limited subset of 5-10 Myr old intermediate-mass stars already close to the main sequence. Hence, in this work an unbiased sample of young stars (<5 Myr) in the intermediate-mass range, $1.5-3.5 M_{\odot}$ are selected to be studied. I use the spectra, optical photometric data and Pre-Main Sequence Evolutionary Tracks to find the parameters like effective temperature, surface gravity, extinction, distance, luminosity, radius, mass and age.

The lines present in the spectra are observed to be correlated with accretion luminosity and the accretion rates are determined. The young nature of the stars are confirmed when they are placed on the HR diagram. It is seen that the younger stars have higher accretion rates compared to the older ones, implying that the accretion rates of the stars decreases as the stars approach the main sequence. This indicates that the accretion rate is an evolutionary property of the Herbig stars. Also, high accretors have significant IR excesses indicating that when discs are young, the stars are young and they have high accretion rates and more excesses; in my sample stars as young as 3 Myr, beyond 3 Myr there is no significant excess and also the accretion rates are low.

Abbreviations

2MASS	2 Micron All Sky Survey
CTTs	Classical T Tauri stars
ESO	European Southern Observatory
EW	Equivalent Width
FUV	Far Ultra-Violet
GMC	Giant Molecular Cloud
HAe	Herbig Ae
HAeBe	Herbig Ae/Be
HBe	Herbig Be
HR	Hertzsprung-Russell
IR	Infrared
IRAF	Image Reduction and Analysis Facility
MA	Magnetospheric Accretion
MK	Morgan-Keenan
MS	Main Sequence
NIR	Near Infrared
PMS	Pre-Main Sequence

SED	Spectral Energy Distribution
SNR	Signal-to-Noise Ratio
UV	Ultra-Violet
UVB	Ultra-Violet and Blue
VIS	Visible
WISE	Wide-field Infrared Survey Explorer
YSO	Young Stellar Object

Contents

1	Introduction	1
1.1	Star formation	1
1.1.1	Herbig Ae/Be stars	5
1.1.2	Protoplanetary Disks	9
1.2	Thesis Intentions	11
2	Characterisation of the stars	13
2.1	Introduction	13
2.2	Observations	16
2.2.1	XShooter Spectrograph	16
2.3	Determination of Parameters	17
2.3.1	Determination of the Temperature and Surface Gravity	18
2.3.2	Determination of Reddening and Scaling Factor	20

2.3.3	Determination of Radius, Mass and Age	23
2.4	HR Diagram and Age	25
3	Accretion Rate and IR Excess Measurements	31
3.1	Introduction	31
3.2	Accretion rate Measurements	33
3.2.1	Equivalent Width Measurements	34
3.3	Accretion Rate vs Stellar Parameters	37
3.4	IR Excess Measurements	43
4	Discussion	50
4.1	Additional Targets	51
4.2	Discussion	51
5	Conclusions	58
5.1	Future Prospects	61
	Bibliography	62

List of Tables

2.1	Table showing the name, RA, DEC, Exposure time in the UVB, VIS and NIR arms, and SNR around H_α line of the targets. . .	27
2.2	Table showing the targets with temperatures and $\log(g)$ obtained for each of the three lines, $H\beta$, $H\gamma$ and $H\delta$, and the last two columns show the effective temperature and surface gravity for each target.	28
2.3	Photometry and distances from the literature, along with the extinction and scaling factor for each target.	29
2.4	The derived stellar parameters.	30
3.1	Equivalent width (EW) measurements of the H_α line for all targets.	47
3.2	Table showing the corrected equivalent width, line luminosity, accretion luminosity and accretion rates of all the targets. . .	48
3.3	IR Excess measurement at K-Band for all the targets.	49
4.1	The stellar parameters for the stars in the literature.	57

List of Figures

1.1	An image showing the different stages during the star formation, [Sahoo, 2016].	3
1.2	An image showing the different stages of evolution of YSOs towards the main sequence, [Palla, 1996].	7
1.3	The figure represents the evolution of a typical disk, [Williams and Cieza, 2011].	11
2.1	Figures showing H_α line of the targets HIP22112 (left) and HIP30448 (right).	14
2.2	Figures showing H_α line of the targets HIP25763 (left) and HIP98992 (right).	15
2.3	An example showing the spectral typing for a target; the target spectra is shown in blue and the Bosz model spectra, denoting the best fit, is shown in orange. $\log(g)$ is in cms^{-2}	19
2.4	Spectral typing for a target showing the lower limit and upper limit of T_{eff} and $\log(g)$ [in cms^{-2}] which fits the spectra; target spectra is shown in blue and the Bosz model spectra is shown in orange.	20

2.5	Photometry fitting of a target, where the Bosz model spectra is shown in blue and the photometric data points are shown in orange; $\log(g)$ is in cms^{-2}	22
2.6	HR diagram with all the stars, along with errors in the measurement of T_{eff} and $\log(L_*)$; the stars with mass lower than $1.5 M_\odot$ are shown in blue dots, the stars in the mass range $1.5\text{-}3.5 M_\odot$ are shown in orange dots and those with mass greater than $3.5 M_\odot$ are shown in green dots. The isochrones and the evolutionary tracks are also shown, where the maroon track shows the evolutionary track of stars of mass $3.5 M_\odot$ and the violet track shows the evolutionary track of stars of mass $1.5 M_\odot$. . .	25
2.7	The age of the stars are plotted against the effective temperature of the stars, where the stars with mass lower than $1.5 M_\odot$ are shown in blue dots, the stars in the mass range $1.5\text{-}3.5 M_\odot$ are shown in orange dots and those with mass greater than $3.5 M_\odot$ are shown in green dots.	26
3.1	The accretion rates of the stars are plotted against their ages; stars with mass lower than $1.5 M_\odot$ are shown in blue dots, stars in the mass range $1.5\text{-}3.5 M_\odot$ are shown in orange dots and those with mass greater than $3.5 M_\odot$ are shown in green dots.	38
3.2	Plot showing \dot{M}_{acc} against T_{eff} , where stars in different mass groups are shown in different colors: blue dots for stars with mass lesser than $1.5 M_\odot$, orange dots for stars in the mass range $1.5\text{-}3.5 M_\odot$ and green dots for stars with masses greater than $3.5 M_\odot$	39
3.3	Plot of accretion rates against the mass of the stars, where the stars younger than 5 Myr are shown in blue dots and the older stars are shown in orange dots.	40

3.4	Plot of accretion rates against the mass of the stars, where stars in different mass groups are shown in different colors: blue dots for stars with mass lesser than $1.5 M_{\odot}$, orange dots for stars in the mass range $1.5\text{-}3.5 M_{\odot}$ and green dots for stars with masses greater than $3.5 M_{\odot}$	41
3.5	The accretion luminosities are plotted against the stellar luminosities, where the stars in different mass ranges are shown in different colors: stars with mass lower than $1.5 M_{\odot}$ are shown in blue, stars in the mass range $1.5\text{-}3.5 M_{\odot}$ are shown in orange and those greater than $3.5 M_{\odot}$ are shown in green.	42
3.6	The figure represents the plot between age and IR excesses of the stars, where stars in different mass ranges are shown in different colors: blue dots represent stars in the range of $1.5\text{-}3.5 M_{\odot}$ and orange dots represent stars with mass greater than $3.5 M_{\odot}$	44
3.7	The figure represents the plot between the accretion rates and IR excesses of the stars, where stars younger than 5 Myr are represented by blue dots and stars older than 5 Myr are represented by orange dots.	45
4.1	The first figure shows T_{eff} vs \dot{M}_{acc} for each target of the sample in this work compared with the values obtained for a selected sample from Fairlamb et al. [2015]; the second figure shows the same targets placed on the HR Diagram with isochrones and evolutionary tracks; The stars younger than 5Myr are shown in blue color and the stars older than 5Myr are shown in orange color.	52

4.2	The figure shows $\log(M_*)$ vs $\log(\dot{M}_{acc})$ for each target of the sample in this work compared with the values obtained for a selected sample from Fairlamb et al. [2015]. The stars younger than 5Myr are shown in blue color and the stars older than that are shown in orange color.	54
4.3	The figure shows $\log(L_*)$ vs $\log(L_{acc})$ for each target of the sample in this work compared with the values obtained for a selected sample from Fairlamb et al. [2015]. The stars younger than 5Myr are shown in blue color and the stars older than that are shown in orange color.	55

Chapter 1

Introduction

Star formation is a very complex process which has occurred countless number of times in the past and is still occurring now. It is important to understand this process to understand the properties of stars and that of the discs around them. This chapter provides a overview of how stars are formed from the giant molecular clouds, and about the protoplanetary disks around them.

1.1 Star formation

Star formation occurs in the clouds of gas in the interstellar medium, called the Giant Molecular Clouds(GMCs). Understanding of GMCs is necessary to understand the process of star formation, as their properties govern the type of stars formed within them. GMCs mainly comprises of molecular hydrogen [Carruthers, 1970], which is not easy to detect due to the absence of emission lines in the radio band and absence of dipole moment [Solomon et al., 1987]. Helium atoms and small amount of other gases and dust are also present in the GMCs. These dust particles absorb all wavelengths shorter than their diameters ($\sim 0.1 \mu\text{m}$) and re-radiate it in the infrared region. The mass of a GMC ranges from 10^4 to 10^7 solar masses, with surface mass density of

about $170 M_{\odot}pc^{-2}$ (Solomon et al. [1979]; Solomon et al. [1987]). They are about 15 - 600 light years in diameter and are very cold with temperatures ranging between 5 - 15K. The largest GMCs are usually present in the very dense regions of the galaxy, while the smaller molecular clouds, called the Bok Globules, are located in the less dense regions [Heyer et al., 2001].

GMCs are the largest cohesive bodies in the galaxies and almost all are producing stars. They consist of filaments and cores within them [Fairlamb et al., 2015]. According to Chira [2018] filaments are made up of gas and dust at high densities. Their length ranges from 1-10pc [Jackson et al., 2010] and are found all through the cold interstellar medium [André et al., 2010].

Cores are regions of dense gas within a molecular cloud which may or may not be associated with a protostellar object [Polychroni et al., 2013]. The core with no star associated is called a prestellar core, which will collapse and form a star, and a protostellar core is when the star has a protostar formed within it [André et al., 2014].

The dense cores are formed when the filament collapses after reaching its critical density [Molinari et al., 2010]. These dense cores are the potential sites of star formation. Stars are formed when these dense cores become gravitationally unstable and collapses [Klessen et al., 2000]. The Jeans mass expression also gives us an understanding of the gravitational stability. Jeans mass is the mass required for a molecular cloud to undergo gravitational collapse. The expression is given by,

$$M_{Jeans} = \left(\frac{5k_bT}{G\mu m_H} \right)^{\frac{3}{2}} \left(\frac{3}{4\pi\rho} \right)^{\frac{1}{2}}$$

where M_{Jeans} is the Jeans mass, k_b is the Boltzmann constant, T is the temperature, G is the Gravitational constant, m_H is the mass of Hydrogen atom, ρ is the density. Initially, the cloud is said to be in hydro-static equilibrium, that is, the cloud remains stable due to the balance of the two forces - the force of gravity acting inwards and the pressure acting outwards. When the force of gravity is more than the outward pressure, gravity wins and the cloud

will experience a collapse [Shu, 1977]. Since the force of gravity is directly related to the mass of the body, higher mass suggests strong gravitational force. When the mass of the cloud exceeds the Jeans mass, it will collapse. The temperature of the collapsing material increases during the collapse due to the release of gravitational potential energy.

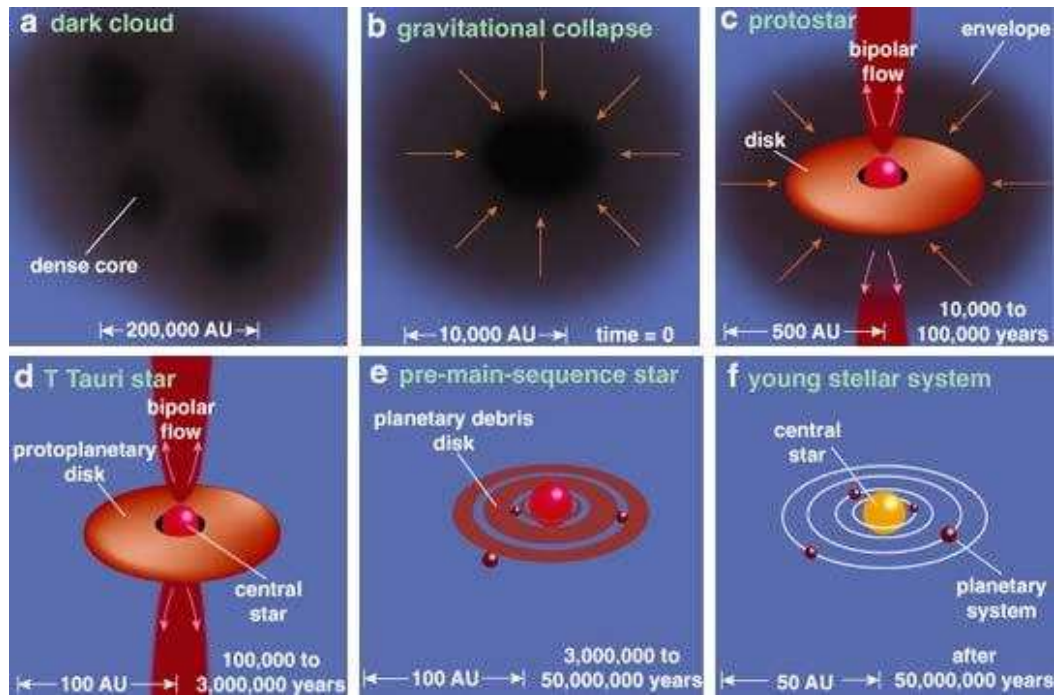


Figure 1.1: An image showing the different stages during the star formation, [Sahoo, 2016].

The cloud doesn't collapse directly to radius = 0. During the initial stages of the collapse, the cloud has a low density and the energy escapes very easily without being absorbed. This phase is called an isothermal collapse as the energy is radiated away. The GMC collapses into small collapsing pieces as the Jeans mass increases due to the increase in the density. Also, as there is an increase in the density the free fall time also falls resulting in an increase in the speed of the collapse. Slowly during the collapse the material becomes optically thick due to an increase in the density. Since no energy can escape, there is an increase in the temperature resulting in an increase in the thermal pressure. This phase is also known as adiabatic collapse. At this point the collapse is ceased and a hydrostatic core is formed. The cloud begins to heat

up as it absorbs all the energy of the collapse. The star at this stage is called a protostar, which is still accumulating Hydrogen atoms. After this stage, the material falling onto the core compresses the core which results in an increase of the temperature within the core [Masunaga et al., 1998]. This increase in temperature causes dissociation of hydrogen, after which the accretion of material onto the surface occurs by free fall and this phase is called the accretion phase.

The rate at which the stars are accreting, accretion rates, is an important parameter as it tells us how the stars are evolving over time. Accretion plays as a source of energy for the emission lines and the UV excess observed in their spectra (Garrison [1978], Donehew and Brittain [2011], Mendigutía et al. [2011]). The presence of emission lines in the spectra, especially at H_α tells us that there is accretion of material from the disc onto the central star. It is also seen that the accretion rates of the stars decreases as they evolve and approach the main sequence [Manara et al., 2016].

During the star formation from the dense cores, the effects of rotation at the dense core level results in larger than observed rotational velocities [Belloche, 2013]. One of the methods that results in conservation of angular momentum is known as magnetic braking [Mouschovias and Paleologou, 1979]. This occurs when there is an increase in local magnetic tension, due to the rotation of the cloud, exerts a braking torque on the cloud. This torque reduces the angular momentum [Nakano, 1989]. The angular momentum can be reduced by another method through the process of accretion discs and outflows. Due to the gravitational instabilities or turbulence, the momentum in the accretion disc can be transferred to the outer part of the disc by torque [Pringle, 1981, Balbus and Hawley, 1991]. On the other hand the outflows of T Tauri stars are seen to be rotating, indicating that the angular momentum is dispersed by the outflows [Bacciotti et al., 2002].

According to the recent observations the GMCs have found to have lifetimes of about 10 to 55 million years [Jefferson and Kruijssen, 2018]. When they are viewed with an optical telescope, they appear dark as they usually do not radiate their own light.

A closest star-forming region is Taurus-Auriga. The region is about 1-2 Myr [Pascucci et al., 2016] and is located at 140pc [Andrews et al., 2013]. This is one of the nearest star-forming regions studied. It lacks the presence of intermediate and high mass stars [Kenyon et al., 2008] but is known to be efficiently forming low-mass star [Monin et al., 2010]. The cloud is about $10^4 M_{\odot}$ and has over 350 known member, which are mainly low mass stellar objects [Rodmann et al., 2006]. Located at around 140pc with a depth of 20pc or more it spans a diameter of about 25 pc [Rodmann et al., 2006].

1.1.1 Herbig Ae/Be stars

Various type of stars fall into the classification of Young Stellar Objects (YSOs) and they show different stages of evolution towards the main sequence. Class 0 protostars, where the SED peaks at sub-millimeter wavelengths, is the earliest stage of the evolutionary phase [Andre et al., 1993]. Class 0 stars are known to be associated with high density region [Sadavoy et al., 2014] and they have strong molecular outflows [Bontemps et al., 1996], whereas that of Class I are much weaker. Classical T Tauri stars and Herbig Ae/Be stars belong to Class II. In this stage an IR excess can be observed, which arises from the disks around them [Sargent and Beckwith, 1987]. These stars have a mass of about 0.1 - 2 M_{\odot} . The final stage of evolution of stars before reaching the main sequence is the Class III stage. The disk in this stage is mostly dispersed away, hence resulting in a small amount of IR excess.

Herbig Ae/Be stars are Pre-Main Sequence (PMS) A-Type or earlier type stars, first identified by Herbig [1960]. They have masses intermediate to that of T-Tauri stars and Massive Young Stellar Objects, which lies in the range of 2 to 10 solar masses. This work focuses on the intermediate-mass Pre-main sequence stars which lie in the mass range of 1.5 - 3.5 solar masses and younger than 5Myr. Herbig stars meet the criteria: “spectral type A or earlier with emission lines, lies in an obscured region, and the star illuminates a fairly bright nebulosity in its immediate vicinity” ([Herbig, 1960][Oudmaijer et al., 2017]) . The luminosities of these objects range from 10 to $10^3 L_{sun}$ and their effective temperatures range from 6,000 - 10,000 K. These stars generally are

accompanied by circumstellar disks, which are made of dust and gas, and an IR excess can be observed which originates from the dust present around the star [van den Ancker et al., 2000].

Based on this IR excess, the Herbig stars can be divided into two groups [Meeus et al., 2001], Group I and Group II. The inner disks of the Group I stars is assumed to be optically thick shielding the rest of the disk and the disk emission can be modelled by a power law [van den Ancker et al., 2000]. On the other hand, in Group II, the inner disk is optically thin resulting in a flared out disk as the outer disk is exposed to stellar radiation. In this case, the resulting disk emission has an added black-body component [van der Plas et al., 2009]. Group I Herbig stars are observed to have gaps in their disks [Maaskant et al., 2013], which could show the beginning of disk dispersal [Alexander et al., 2014]. Hollenbach et al. [1994] suggests that the disk dispersal occurs mainly due to photo-evaporation. But it could also be due to the clearing of the orbital planets [Dodson-Robinson and Salyk, 2011].

These stars are accreting mass from the inner regions of the disks around them and their accretion rates can be measured. Within the theory of magnetospheric accretion (MA), the accretion rates can be determined from the measured UV excess [Muzerolle et al., 2004]. But this theory couldn't be applied to all Herbig stars as all Herbig stars don't have strong magnetic fields. However, only if the strength of the magnetic field of the central star is adequate to truncate the material onto the star, MA can be applied to such stars [Shu et al., 1994]. The context of MA is applicable to CTTs which have magnetic fields of strengths of the order of 10^3 Gauss [Bouvier et al., 2007].

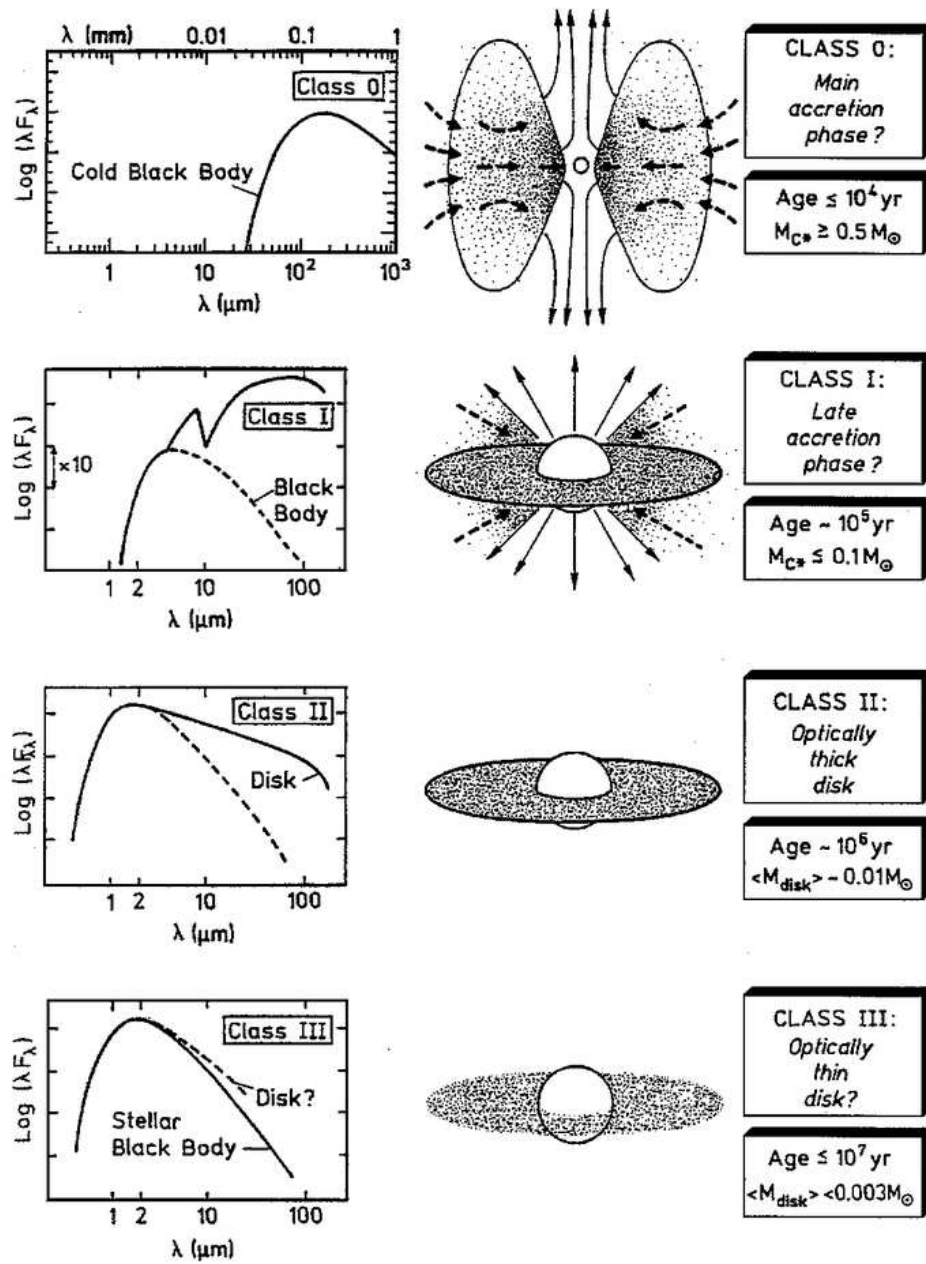


Figure 1.2: An image showing the different stages of evolution of YSOs towards the main sequence, [Palla, 1996].

The PMS evolution phase for these kinds of stars is less than 10Myr [Bressan et al., 2012]. The material of the disks around these stars gradually reduces in quantity: most of it gets accreted on to the star and some is lost due to photo-evaporation [Fairlamb et al., 2017]. During the PMS evolutionary phase, the stars' interior is too cold for the fusion reaction to occur and only

gravitational energy is in action at this point; the fusion of hydrogen to form helium occurs only when the star reaches the main sequence. Strom et al. [1972] observed that the main sequence stars have higher surface gravities than the Herbig stars. Surface gravity is the acceleration due to gravity experienced by a hypothetical particle of negligible mass which is located very close to the surface of the star. By calculating the surface gravities of the stars, we can calculate their age, i.e., know their position on the HR diagram.

A number of work shows that the Herbig Ae stars are different from Herbig Be stars, but are similar to T Tauri stars [Oudmaijer et al., 2017]. It was found by Cauley and Johns-Krull [2015] that the absorption and emission line properties are different for Herbig Ae and Herbig Be stars. T Tauri stars and Herbig Ae stars were found to have similar linear spectropolarimetric properties, but that of Herbig Be stars was found to be different because the strength of magnetic fields is different in both Herbig Ae and Herbig Be stars [Vink et al., 2005]. According to Järvinen et al. [2016], the magnetospheric accretion causes spectroscopic variability in a Herbig Ae star.

Spectral classification plays an important role in the study of stars. In general, PMS A-type stars have the effective temperature of 7,500 - 10,000K. The Morgan - Keenan (MK) system subdivides these stars into ten classes of spectral type, A0 to A9, A0 being the hottest and A9 the coolest. These stars have strong Balmer lines accompanied by many faint to moderately strong metallic lines, whose strength gradually increases from A0 to A9. Hydrogen has its maximum strength at A2 and decreases from there.

The spectral type determination will help us gather information about the total extinction due to the dust, the type of the star, and the components of the dust. Many of the stars show large extinction due to the presence of dust in the star formation region and the presence of significant amounts of dust in the disk around the star [Palla and Stahler, 1994]. The spectra of these stars show some peculiarities, like the excess emission in the infrared region provides an evidence for the presence of the disks around them [Fairlamb et al., 2017], and the presence of strong emission at hydrogen alpha lines shows that the star is still accreting [Kraus et al., 2008]. The broadening of the absorption

lines of the Herbig Ae stars yields the rotational speeds [van der Plas et al., 2015].

1.1.2 Protoplanetary Disks

Almost every young star has a disk around it which is formed when the gas and dust settles into a circumstellar orbit [Lin, 2019], during the gravitational collapse of a molecular cloud [Williams and Cieza, 2011]. Most of their mass, around 99%, is in the form of gas, mainly molecular hydrogen, and around 1% is dust. The disk around young stars can have radius up to 1000 au [Panic, 2009]. The lifetime of such disks is generally around several million years [Fedele et al., 2010]. During this time, apart from losing some material due to accretion onto the star, some is lost through outflows and photo-evaporation, and some condenses into planetesimals [Ercolano and Pascucci, 2017].

The presence of an excess emission in the IR confirms the presence of circumstellar material around the stars as the stars radiate mainly in the IR; though the disk is made of cool dust and gas, some of the dust grains gain energy from the star, at UV, and the disk radiates at IR ([Peretto et al., 2013][Greenwood et al., 2019]). Through these observations we can measure properties like mass, size, composition and structure. The disks have lifetimes which range from 1 to 10 Myr and they are found to dissipate faster around high mass stars than solar mass stars, and much slower around very low mass stars [Williams and Cieza, 2011].

During the initial stages of the collapse of the molecular cloud, the disk mass does not increase as the material in the disk is rapidly funnelled onto the star. There is continuous accretion onto the star due to the internal friction [Wiebe, 2018]. Gradually as the material is used up or is dispersed, due to accretion onto the star or photoevaporation, the accretion is reduced, and some amount of the material persists. As the radius of the collapsing cloud decreases, the rotation speed is increased due to conservation of angular momentum [Williams and Cieza, 2011]. The cloud gradually flattens by collapsing in the vertical direction and gains the shape of the disk [Birnstiel et al., 2010].

All disks do not follow the same evolutionary phase, though most of them follow a similar path. The figure 1.3 shows the evolution of a typical disk. During the initial stages of the evolution of the disks, it loses its material due to accretion onto the star and photoevaporation of the outer disk by far-UV by the star, hence losing its mass [Gorti et al., 2009]. The size of the disk is limited to hundreds of AU due to the FUV driven photoevaporation. This is represented in figure 1.3a.

This stage lasts for a few millions of years often manifests itself as a flared disk. Figure 1.3b shows the next stage where the disk is flatter, when the grains increase in their size and settle down on the plane of the disk. After this stage, there is a decrease in the accretion onto the star as the outer disk does not provide material to the inner regions of the disk. Since no material is present in the inner regions of the disk, a hole is formed, which is about a few au in size. Initially at this stage, the photoevaporation increases as the photons from the star can penetrate through the inner regions of the disk, this is shown in figure 1.3c. The last part the figure, 1.3d, shows the debris disk formed, which has very low mass compared to the earlier mass of the disk. The debris disk is formed after the photoevaporation of the remaining gas after the previous stage. The radiation pressure removes the smaller grains and only the large grains and planetesimals are left in the disk [Dullemond and Dominik, 2005].

Planet formation occurs within the protoplanetary disks. Initially planetesimals are formed which gives rise to small planets after millions of years. This happens due to the accumulation of dust grains from the ISM. Gradually the gas contents in the disk depletes when certain planets, like Jupiter and Saturn, gathers gases from the disks to form thick atmospheres. Giant planets are formed mostly around stars of mass $2M_{Sun}$ [Reffert et al., 2015]. The protoplanetary disk slowly evolve and the evolution depends on the mass of the star it is around [Gorti and Hollenbach, 2009]. The rate of evolution is higher around high mass stars [Ribas et al., 2015].

Around old stars ($> 3 M_{\odot}$), with age in the range > 10 million years, disks have lost majority of the gas contents and such disks with dust are called debris disks [Hughes et al., 2018]. Since the stars are very old and also that the dust

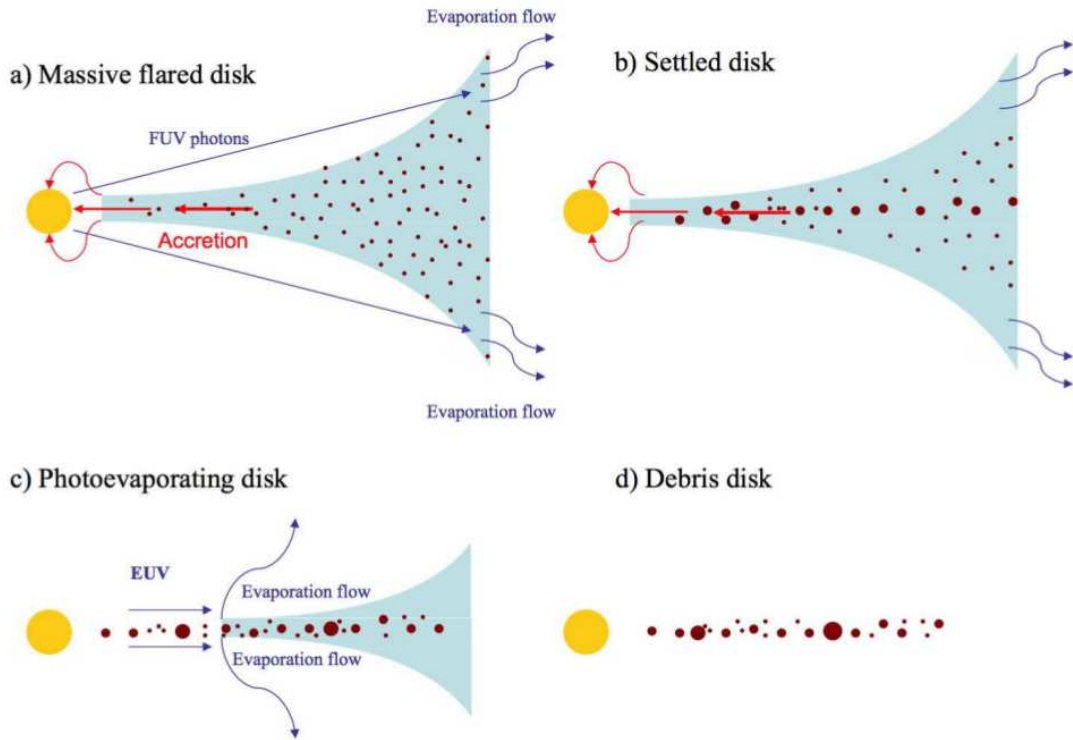


Figure 1.3: The figure represents the evolution of a typical disk, [Williams and Cieza, 2011].

has a shorter lifetime, the dust present in the debris disks is thought to be formed from the collisions of the planetesimals present in the disk, signalling that debris disks might be a later stage of the disk evolution.

1.2 Thesis Intentions

The introduction chapter was an overview of the star formation, Herbig stars and the disks around them. This thesis deals with characterising a sample of 18 young Pre-Main Sequence (PMS) stars intermediate mass stars by following a homogeneous approach to determine their temperature, surface gravity, extinction, luminosity, mass, age and radius, and determining their accretion rates by measuring the equivalent widths of the Hydrogen-alpha emission line and also calculating the IR excesses for the stars.

The Chapter 2 is concerned with the methods involved in determining the stellar parameters. First, the temperature and surface gravity are determined by fitting the spectra of the star with that of a model. Then using this temperature the reddening and the scaling factor are determined. Once this is known, the luminosity of the star can be calculated as the distance of the star is known. Using the luminosity and the temperature in the Lionel-Siess PMS evolutionary tracks, the mass, age and radius are determined. This part of the work is very important as it forms the basis in determining the accretion rates for the sample.

Chapter 3 focuses on accretion rate and IR excess determinations. The equivalent widths of the Hydrogen-alpha emission line is used along with the determined parameters in the previous chapter to determine the accretion rate. The equivalent width is used to determine the line flux and the line luminosity is calculated using this. Accretion luminosity is calculated and using this the accretion rate is determined. This chapter also shows how various parameters vary with the accretion rates. To determine the IR excess, the ratio of the dereddened observed flux and photospheric flux values at K band is used.

Chapter 4 includes the additional targets from the archive for which the accretion rates were studied and it involves the discussion and comparison of the results obtained with the existing studies on young Intermediate mass PMS stars. Chapter 5 is the conclusion and future prospects.

Chapter 2

Characterisation of the stars

2.1 Introduction

This thesis focuses on the study of Herbig Ae stars younger than 5Myr and in the mass range 1.5-3.5 solar masses. The frequency of formation of giant planets is the highest around stars of mass around $2M_{\odot}$ ([Reffert et al., 2013], [Quirrenbach et al., 2015]), and around stars above $1.5M_{\odot}$ the orbits of giant planets are larger than 1 au [Sato et al., 2008]. This gives us information about the dispersal of the protoplanetary disc around the stars; giant planets can only form and migrate in presence of dense gas ([Nelson and Papaloizou, 2004], [Papaloizou et al., 2004]). A hypothesis was stated by Kennedy & Kenyon 2008 that faster clearing of the inner disc due to photoevaporation around intermediate-mass stars might halt the migrating giant planets before they reach smaller orbital distances and such planets are found around low mass stars. This tells us that low mass and intermediate-mass stars evolve differently on the pre-main sequence. Intermediate-mass stars are more luminous and their photoevaporation is driven by FUV photons, unlike X-rays in case of low-mass stars [Gorti and Hollenbach, 2009]. The thermal and chemical evolution of the discs are also different due to the large luminosities [Panić and Min, 2017]. The near-IR excess of the stars are studied to check the inner

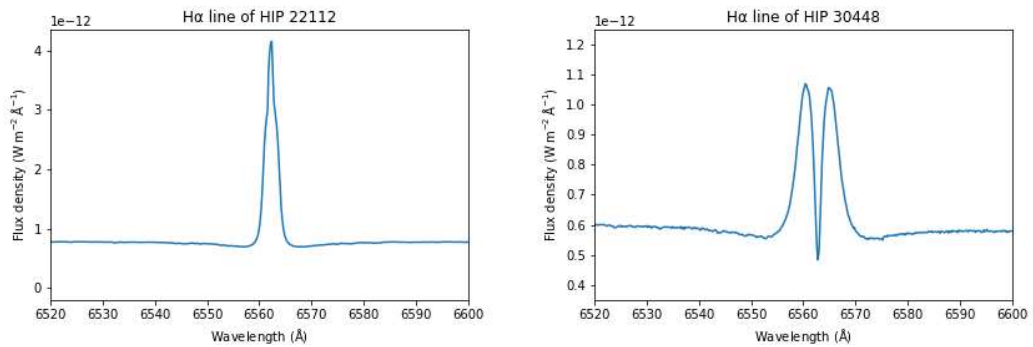


Figure 2.1: Figures showing H_{α} line of the targets HIP22112 (left) and HIP30448 (right).

disc evolution around intermediate-mass stars. This work deals with measuring the stellar parameters, mass accretion rates and IR-excess to check how intermediate mass star evolves.

The sample was collected using the Tycho-GAIA Astrometric Solution catalogue and Hipparcos catalogue, by keeping the declination between -78° and $+30^{\circ}$, and across all right ascension. First the stars with precise B and V photometry were selected. Next only stars with measured excess levels $F_{total}/F_{midIR} \geq 1$ were considered. This limit corresponds to debris disc level of excess at $20\mu\text{m}$ [Marino et al., 2017], and therefore we do not expect detectable signatures of accretion with XShooter below this level. Further the stars were selected based on their location on the HR diagram, keeping stars which may have the young age of ≤ 5 Myr and in the mass range $1.5\text{-}3.5 M_{\odot}$. There are studies in the literature about pre-main sequence stars to see how the solar mass and intermediate-mass stars evolve. However, more complete samples of young pre-main sequence stars are not present to quantify the difference as there is no unbiased statistical sample of pre-main sequence stars in the intermediate-mass stellar range in the literature. Most current studies in the stellar range of intermediate-mass focuses on the Herbig Ae population, a limited subset of 5-10 Myr old intermediate-mass stars already close to the main sequence. Hence, in this work an unbiased sample of young stars (< 5 Myr) in the intermediate-mass range, $1.5\text{-}3.5 M_{\odot}$ are studied. The UVB, optical and near-IR spectra of about 200 pre-main sequence candidate stars are obtained, out of which a subset of 18 stars are found to be accreting. This

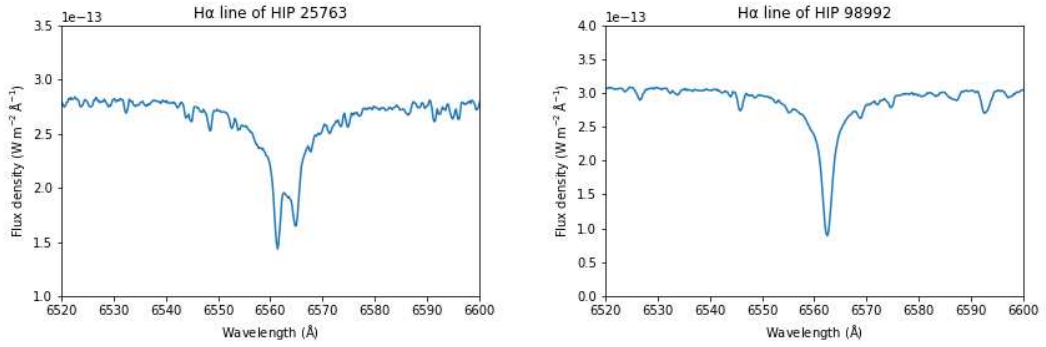


Figure 2.2: Figures showing H_{α} line of the targets HIP25763 (left) and HIP98992 (right).

was determined by checking for emission at hydrogen alpha (H_{α}) line of the Balmer series; only stars which are accreting will have emission at H_{α} line. The figures 2.1 and 2.2 shows examples of 4 targets showing their H_{α} lines: HIP 22112 shows strong emission indicating that it is strongly accreting, HIP 30448 and HIP 25763 shows the presence of both emission and absorption indicating some accretion happening and HIP 98992 shows no emission indicating that it is not accreting. Also, 27 targets were excluded from the observed sample as their data was already present in the ESO archive and they will analysed together with our 18 targets.

In order to accurately determine the accretion rates and the IR excesses of the stars, it is necessary to follow a homogeneous approach to accurately measure the stellar parameters [Fairlamb, 2015]. Many methods have been proposed by Mora et al. [2001] and Hernández et al. [2004], yet the most preferred one is the method used by Montesinos et al. [2009], as it doesn't involve knowing the distances of the stars for the calculation of other parameters.

This chapter uses the homogeneous approach followed by Montesinos et al. [2009] to determine the stellar parameters like the stellar temperature, surface gravity, extinction, luminosity, mass, age and radius for a sample of 18 PMS candidate intermediate mass stars. To achieve this goal, the UVB, Optical(VIS) and near IR(NIR) spectra of the sample is used which was obtained using the X-Shooter spectrograph. This chapter is important in order to determine the accretion rates, discussed in the next chapter.

2.2 Observations

2.2.1 XShooter Spectrograph

X-Shooter echelle spectrograph was used to collect data that is required for this project. X-Shooter is a multi-wavelength, intermediate resolution spectrograph mounted at the VLT, Cerro Paranal, Chile. It provides spectra covering a large wavelength range, from the ultraviolet (UV) to the near-infrared (NIR), taken simultaneously across the three arms: the UVB arm (3000-5600 Å), the VIS arm (5600-10200 Å) and the NIR arm (10200-24800 Å) [Vernet et al., 2011]. Each of the three arms is an individual echelle spectrograph, which disperses the incident beam of light in the form of a spectrum. Depending on the slit width and the wavelength, it operates at the resolution of about 4000-17000. The data reduction package provides a fully calibrated 2-dimensional spectra over the entire wavelength range. The data was automatically reduced by the ESO pipeline and were checked by collaborator, by Dr. Mario van den Ancker at ESO before delivering it to us.

The spectra were obtained with $S/N > 100$ over the entire wavelength range (3600-24800 Å) for each target in the sample. The SNR around the H_α line of the Balmer series is shown in Table 2.1. The exposure times for each target varies in the three arms: UVB, VIS and NIR and are shown in the table below, along with their coordinates, Right Ascension and Declination.

2.3 Determination of Parameters

As discussed earlier, the parameters are determined by following the approach explained by Montesinos et al. [2009]. Three major steps are followed to determine the parameters:

- First, spectral typing of the XShooter spectra with the spectra from the BOSZ model [Bohlin et al., 2017] is done to obtain the stellar effective temperature, T_{eff} , and surface gravity, $\log(g)$.
- Second, the obtained temperature determined using the BOSZ model along with the values of the B, V and R photometric data points from the literature is used to determine the reddening of the spectra, A_V , and the scaling factor, which is the ratio of the distance and the radius (D/R_*) for all the targets. Knowing the scaling factor helps us calculate the radius of the stars, as their distances are already known.
- The third step is the final step in determining the parameters. In this step, first the luminosity of the star is calculated using the above determined data. Using the luminosity and the effective temperature in the Pre-Main Sequence Evolutionary tracks [Siess et al., 1997], the other parameters like mass, radius and age of the stars are determined.

Each of the above steps are discussed in detail in the following sections of the chapter, together with the results obtained.

2.3.1 Determination of the Temperature and Surface Gravity

Since the XShooter instrument covers a large wavelength from 3000 Å to 24800 Å, it allows us to derive the values of the effective temperature and the surface gravity for all the 18 targets. The method similar to that used by Montesinos et al. [2009] is used in order to achieve it. The hydrogen Balmer lines are sensitive to changes in both T_{eff} and $\log(g)$. Since emission can be seen in the core, the wings of these lines are used to perform spectral typing. Among the hydrogen Balmer lines, H_α is the strongest and broadest of the series for Herbig stars and they often exhibit emission and can affect the parameters derived. Hence, H_β , H_γ and H_δ lines are used to determine T_{eff} and $\log(g)$ for the targets.

The BOSZ model [Bohlin et al., 2017] is used to perform the spectral fitting. To compare the lines from the spectra of the stars, the same lines from the model are also normalised based on the continuum on both the sides of the line in the same wavelength region. This normalisation is done using IRAF (Image Reduction and Analysis Facility) software. The comparison of the observed spectra to that of the model is done by over-plotting the lines and setting the T_{eff} to increase in steps of 250K and of $\log(g)$ to increase in steps of 0.5 cm s^{-2} . The best fit is chosen based on the wings on both sides of the lines where intensity is greater than 0.8, to avoid any effect of emission and rotational broadening of the line, which affects the central parts of the absorption lines.

Since fitting is performed for three lines of the hydrogen Balmer series, there are possibilities that the value of T_{eff} and $\log(g)$ obtained for each line might be different resulting in three different temperatures for an individual star. In such case, the best of the three fits is considered as the stellar effective temperature and surface gravity. The best fit is chosen by visually comparing the fits. Sometimes, more than one combination of temperature and surface

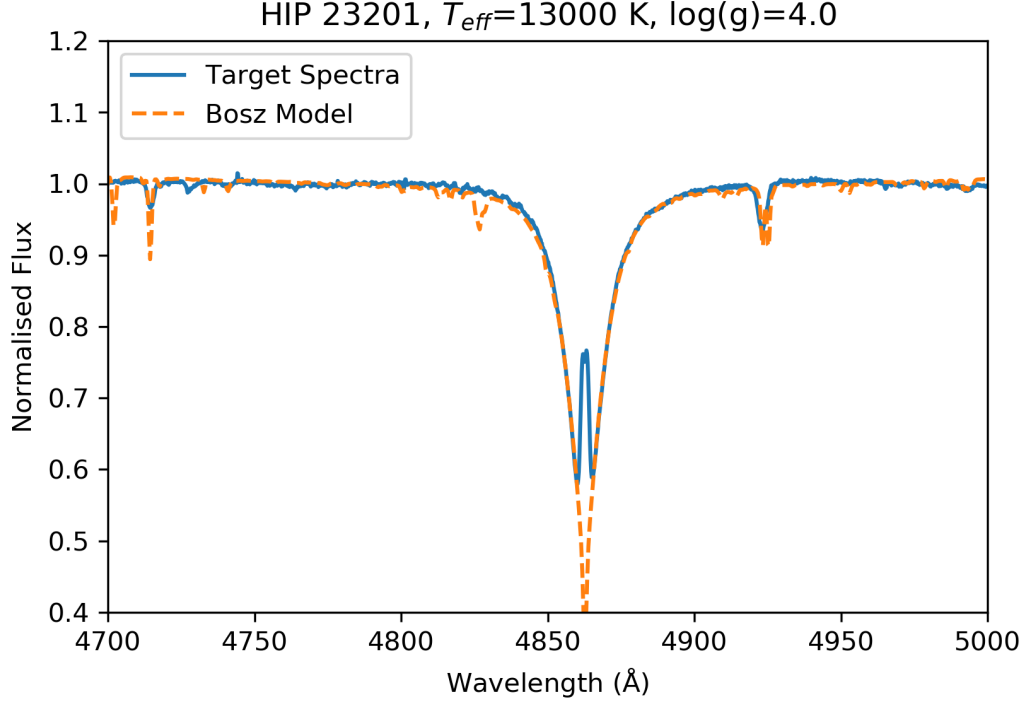


Figure 2.3: An example showing the spectral typing for a target; the target spectra is shown in blue and the Bosz model spectra, denoting the best fit, is shown in orange. $\log(g)$ is in cm s^{-2} .

gravity can fit to the spectra. In such cases, the other non-Hydrogen absorption lines present are considered to see which combination of T_{eff} and $\log(g)$ fits the other lines as well. This gives the errors in the measurement of T_{eff} and $\log(g)$. The best fit is shown in Fig 2.3. Fig 2.4 shows the upper and lower limits of the temperatures. Table 2.2 shows the values obtained for each individual line and then the final T_{eff} and $\log(g)$. The spectra from the model corresponding to the T_{eff} and $\log(g)$ is used to perform fitting of the photometric data points with the model spectra to obtain extinction and scaling factor. The effective temperature and luminosity is used to obtain other parameters like mass, radius and age. Hence, the calculation of the errors in the measurements of T_{eff} and $\log(g)$ is necessary to obtain the errors in other parameters.

Though this method of performing the spectral typing is more convenient and yields good results, sometimes there can be a few issues. Firstly, if the spectra of the star displays extreme emission lines it becomes difficult to fit the lines

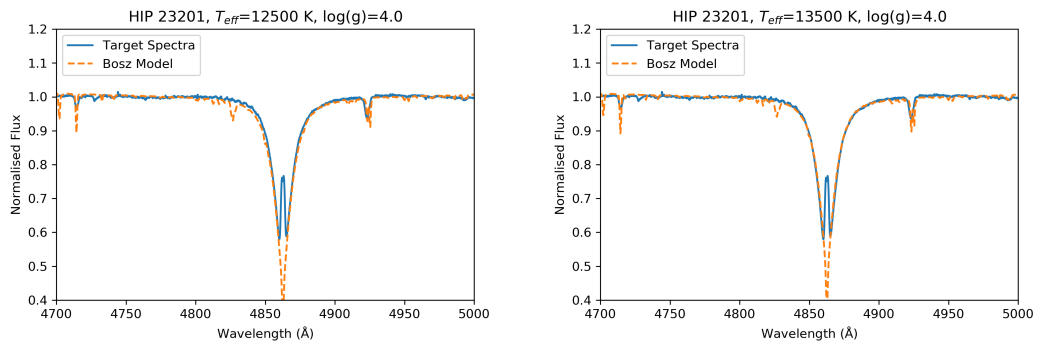


Figure 2.4: Spectral typing for a target showing the lower limit and upper limit of T_{eff} and $\log(g)$ [in cm s^{-2}] which fits the spectra; target spectra is shown in blue and the Bosz model spectra is shown in orange.

based on the continuum, as the line strength will be strong across the Balmer series and the width of the lines covers the photospheric absorption wings [Fairlamb, 2015]. Another issue can arise due to the non-linear relationship between the width of the Balmer lines and the surface gravity. This makes the fitting of the target spectra with the spectra of the model difficult for stars with $T_{eff} < 9000\text{K}$ [Guimarães et al., 2006] due to the degeneracy. For example, HIP 25763, HIP 57027, TYC 461-622-1 and TYC 9329-60-1 have their temperatures below 9000K, and the lines are broader. Below 9000K, the line width increases with decrease in surface gravity. It was difficult to perform fitting for these targets as two different temperatures had the same width but different values of surface gravity. Then, the best fit was chosen by the presence of the other non-Hydrogen lines.

2.3.2 Determination of Reddening and Scaling Factor

Interstellar reddening occurs due to the presence of the interstellar dust which absorbs and scatters blue light photons more than red light photons, thus making the stars appear redder than they actually are. This step deals with determining the reddening of the spectra of the targets using the temperature obtained in the previous step. To do this the spectra of the model, based on the determined temperature, is fitted with the observed optical photometry,

taken from the literature.

By performing the fitting, the interstellar reddening A_V , and the scaling factor D/R_* , which is the ratio of the distance of the star to its radius, can be determined. The scaling factor is a result of fitting the the observed photometric data with the model [Bohlin et al., 2017]. To perform the fitting, the B, V, and R points, at 4400 Å, 5500 Å and 6400 Å, are used in this work. Photometry of the I band can also be used, but for the list of targets worked on in this project the photometry at I band was not available in literature, hence only B V and R bands are used. The Balmer excess can have an influence on the U band and hence it is a better option not to consider that to perform fitting. Also, long-wards of the I band, there can be an influence of IR excess, and no photometry after this is used. So, choosing only B, V, R and I bands would be ideal. In this work, the photometry is assumed to be mainly photospheric and the effect for variability is low. The photometric values with maximum brightness are chosen, in case there are many photometric values. The effect of variability on Herbig stars have been observed in many earlier works like Mendigutía et al. [2013], Oudmaijer et al. [2001], but it has been observed that it is mostly less than 0.1 mag in majority of the stars [de Winter et al., 2001].

The stellar effective temperature and surface gravity obtained in the previous step is used to do the fitting. The photometry points are fit with the Bosz model spectra [Bohlin et al., 2017]. To do this, the relationship between the flux and the observed photometry is used. Both A_V and D/R_* are simultaneously determined and to obtain the best fit A_V is increased in steps in 0.01 and D/R_* in steps of 0.1. The equation relating the observed photometry and flux is represented in equation 2.1 and the equation relating the flux and the scaling factor is shown in equation 2.2.

$$F_1 = F_0 * 10^{\frac{A_{const.} * A_V - obs.mag}{2.5}} \quad (2.1)$$

F_1 is the flux calculated using the observed photometry, F_0 is the zero magnitude flux, $A_{const.}$ is the reddening constant which is 1.34, 1.00 and 0.75 for

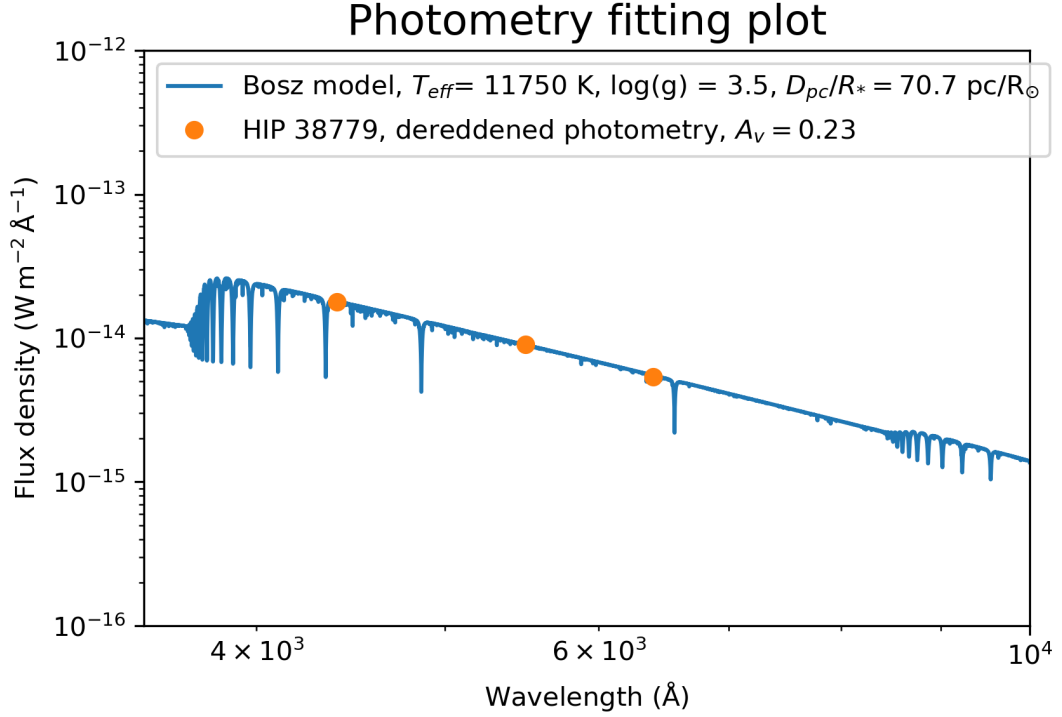


Figure 2.5: Photometry fitting of a target, where the Bosz model spectra is shown in blue and the photometric data points are shown in orange; $\log(g)$ is in cm s^{-2} .

A_B , A_V , A_R in B V and R bands respectively [Cardelli et al., 1989], and the observed magnitude (obs. mag) is the observed photometric data point.

F_{surface} , the surface flux is given by

$$F_{\text{surface}} = \frac{L_*}{4\pi R_*^2} \quad (2.2)$$

F_2 is the flux at the distance D and is given by,

$$F_2 = \frac{L_*}{4\pi D^2} \quad (2.3)$$

By comparing equation 2.2 and equation 2.3, we get,

$$F_2 = \frac{F_{surface}}{\left(\frac{D}{R_*}\right)^2} \quad (2.4)$$

F_2 is the flux from model, $F_{surface}$ is the surface flux, D is the distance of the stars in parsec and R_* is the radius of the star in terms of radius of the sun.

The best fit to the photometry is obtained when the observed photometry is in-line with the Spectral Energy Distribution (SED) shape of the model; an example is shown in the figure 2.5. Since the distance of the stars is known, the radius of the star can be calculated from the scaling factor determined in this step. The table 2.3 shows the distances taken from GAIA catalog [Gaia Collaboration, 2018] and the photometry, with their references. The determined A_V and D/R_* is shown in the table , along with the errors in their calculations. The errors are obtained by determining the values of extinction and scaling factor for the upper and lower limits of the temperature.

2.3.3 Determination of Radius, Mass and Age

This is the final step of determination of the other stellar parameters like luminosity, radius, mass and age for the targets. The stellar effective temperature, surface gravity, reddening and scaling factor are determined in the previous steps. Since the distance is known, the radius of the star can be calculated from the scaling factor. Once the temperature (T_{eff}) and radius (R_*) is known, the luminosity of the star can be calculated, as L_* . The formula used is $L_* = 4\pi R_*^2 \sigma T_{eff}^4$. The errors in both T_{eff} and R_* are used to compute the errors in the calculation of luminosity, which will then be used to calculate the errors in the other parameters. The Pre-Main Sequence (PMS) Evolutionary Tracks [Siess et al., 1997], are used to determine the other parameters.

Each evolutionary track denotes a fixed mass, showing how a star would contract and evolve over time, changing its temperature and luminosity. The change in these parameters results in a change in mass, radius and age as well.

The metallicity is kept $Z=0.01$ for all the targets in this work. The temperature (in K) and luminosity (in L_{\odot}) are entered and metallicity is chosen to be $Z=0.01$. The radius, mass and age of the stars are determined.

The errors in the measurements of T_{eff} , $\log(g)$, A_V and D/R_* are obtained in the previous steps. Since the distance is known, the errors in the measurement of radius is determined using the upper and lower limits of the scaling factor. Similarly, errors in the values of luminosities is determined using the errors in radius and effective temperature. Then the errors in mass, radius and age are determined, using the upper and limits in temperature and luminosity in the PMS Evolutionary Tracks. By this, the errors in the measurements of all the parameters are determined.

By this point, all the basic parameters of the stars are determined. The following table 2.4 shows all the derived parameters, along with the errors in their measurements. With the parameters known, it is possible to place the stars on the HR Diagram.

2.4 HR Diagram and Age

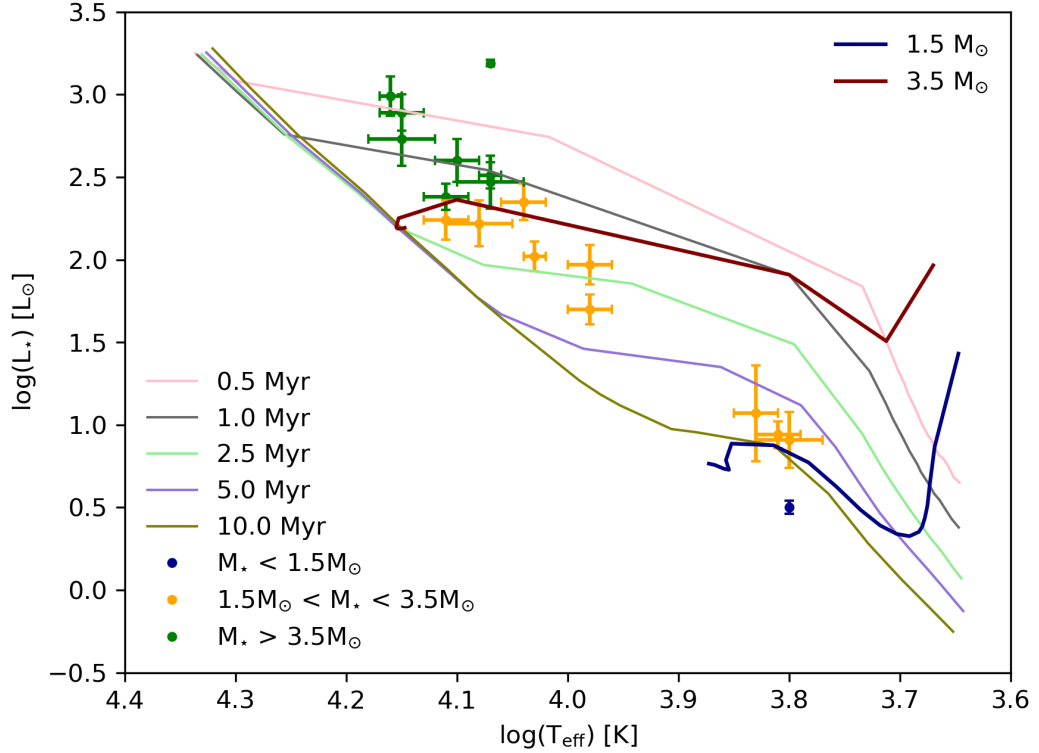


Figure 2.6: HR diagram with all the stars, along with errors in the measurement of T_{eff} and $\log(L_*)$; the stars with mass lower than $1.5 M_\odot$ are shown in blue dots, the stars in the mass range $1.5\text{--}3.5 M_\odot$ are shown in orange dots and those with mass greater than $3.5 M_\odot$ are shown in green dots. The isochrones and the evolutionary tracks are also shown, where the maroon track shows the evolutionary track of stars of mass $3.5 M_\odot$ and the violet track shows the evolutionary track of stars of mass $1.5 M_\odot$.

Using the T_{eff} and L_* determined using the spectra, the stars can be placed on the HR Diagram. The figure 2.6 shows all the targets placed on the HR diagram, with the isochrones and evolutionary tracks also shown. The age of the stars were determined using the PMS Evolutionary tracks [Siess et al., 1997]. Fig 2.7 shows how the temperature varies with the age of the stars, both of which were determined in this chapter. The criteria we are interested in working is that the targets are younger than 5Myr and in the mass range $1.5\text{--}3.5 M_\odot$. Most current studies focus on a limited subset of 5-10Myr intermediate-mass stars. Hence, the criteria chosen in this work provides an

unbiased sample of young intermediate-mass stars. Amongst the entire list of targets in this work, 9 out of 18 are in the required mass range. The placement of these stars on the isochrones and evolutionary tracks confirm their young nature, as 6 out of the 9 stars in the required mass range (shown in Fig 2.5 in orange dots) are seen to be younger than 5Myr, while the other 3 are 5-10Myr old. Stars with their mass greater than $3.5 M_{\odot}$ are found to be around 1Myr and there is only one star in the sample which has mass lower than $1.5 M_{\odot}$ which is older than 10Myr. It is seen that more massive stars are more luminous than lower mass stars. In figure 2.6, it is seen that the older stars are usually cooler than the younger stars, i.e. the hottest stars are the youngest ones. This is a consequence of the fact that the stars with lower masses evolve towards the main sequence slower than the higher mass stars. Also, as seen in the literature, the PMS evolutionary phase for hotter stars is shorter than for cooler stars.

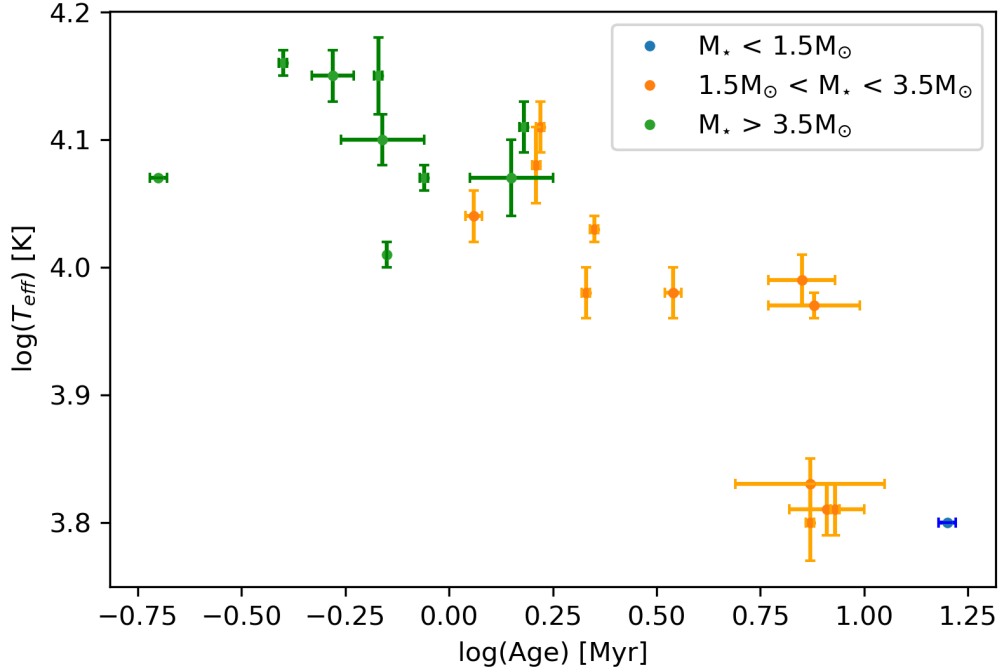


Figure 2.7: The age of the stars are plotted against the effective temperature of the stars, where the stars with mass lower than $1.5 M_{\odot}$ are shown in blue dots, the stars in the mass range $1.5 M_{\odot}$ – $3.5 M_{\odot}$ are shown in orange dots and those with mass greater than $3.5 M_{\odot}$ are shown in green dots.

Table 2.1: Table showing the name, RA, DEC, Exposure time in the UVB, VIS and NIR arms, and SNR around H_{α} line of the targets.

Name	RA (J2000)	DEC (J2000)	Exposure time (s) UVB	Exposure time (s) VIS	Exposure time (s) NIR	SNR
HIP 22112	04:45:34.68	+19:19:41.9	360	300	450	144.81
HIP 23201	04:59:35.63	+25:48:26.9	360	300	450	382.70
HIP 25763	05:30:05.99	+29:33:10.1	360	300	450	72.96
HIP 28561	06:01:41.63	+22:24:03.6	40	80	80	174.44
HIP 29635	06:14:41.94	-73:37:35.4	60	60	140	117.84
HIP 30448	06:24:02.28	+08:53:06.0	40	40	80	167.56
HIP 38779	07:56:15.77	-61:05:57.9	60	60	140	154.52
HIP 48613	09:54:51.23	-50:14:38.3	40	40	80	211.55
HIP 57027	11:41:32.57	-77:03:16.8	60	60	140	129.85
HIP 57143	11:43:07.72	-72:26:43.8	120	120	200	148.25
HIP 61738	12:39:14.49	-75:22:14.0	40	40	80	142.49
HIP 74911	15:18:31.99	-47:52:30.7	12	12	20	164.18
HIP 77289	15:46:47.37	-52:08:46.2	120	120	200	161.36
HIP 81710	16:41:23.11	-68:17:46.0	40	40	80	168.57
HIP 92364	18:49:26.65	-11:47:18.5	240	200	300	287.52
HIP 94260	19:11:11.24	+15:47:15.5	120	120	200	193.93
TYC-461-622-1	18:57:45.00	+05:56:30.2	240	200	300	51.50
TYC-9329-60-1	20:53:24.07	-71:50:13.8	240	200	300	58.74

Table 2.2: Table showing the targets with temperatures and $\log(g)$ obtained for each of the three lines, $H\beta$, $H\gamma$ and $H\delta$, and the last two columns show the effective temperature and surface gravity for each target.

Name	β T(K)	β (cm/s^2)	γ T(K)	γ (cm/s^2)	δ T(K)	δ (cm/s^2)	T_{eff} (K)	$\log(g)$ (cm/s^2)
HIP 22112	14500	3.5	14500	4.0	14000	4.5	14500^{+500}_{-500}	$4.0^{+0.50}_{-0.50}$
HIP 23201	13000	4.0	13000	4.0	13500	3.5	13000^{+500}_{-500}	$4.0^{+0.00}_{-0.50}$
HIP 25763	6250	4.5	6250	4.5	6750	5.0	6250^{+500}_{-250}	$4.5^{+0.50}_{-0.00}$
HIP 28561	12000	4.0	11750	4.0	11500	4.5	11750^{+750}_{-000}	$4.0^{+0.50}_{-0.00}$
HIP 29635	11250	3.5	11000	3.5	10750	3.5	11000^{+500}_{-500}	$3.5^{+0.00}_{-0.00}$
HIP 30448	12000	3.5	11750	3.5	11500	4.0	11750^{+250}_{-250}	$3.5^{+0.50}_{-0.00}$
HIP 38779	11750	3.0	11750	3.5	11500	3.5	11750^{+000}_{-500}	$3.5^{+0.00}_{-0.50}$
HIP 48613	9750	4.5	9250	4.0	9500	4.0	9500^{+500}_{-500}	$4.0^{+0.00}_{-0.50}$
HIP 57027	6750	5.0	6750	4.5	7000	4.5	6750^{+250}_{-250}	$4.5^{+0.50}_{-0.00}$
HIP 57143	14000	3.5	14000	4.0	13500	4.5	14000^{+500}_{-500}	$4.0^{+0.50}_{-0.50}$
HIP 61738	13000	4.0	13000	4.0	13000	4.0	13000^{+500}_{-500}	$4.0^{+0.00}_{-0.00}$
HIP 74911	12500	4.0	12000	4.0	11750	4.5	12000^{+1000}_{-250}	$4.0^{+0.50}_{-0.00}$
HIP 77289	12500	4.0	13000	3.0	12000	3.5	12500^{+500}_{-750}	$3.5^{+0.50}_{-0.50}$
HIP 81710	14500	4.0	14000	4.0	14000	4.0	14000^{+1000}_{-500}	$4.0^{+0.00}_{-0.00}$
HIP 92364	10750	3.5	11000	3.5	10500	4.0	10750^{+250}_{-250}	$3.5^{+0.50}_{-0.00}$
HIP 94260	9750	4.5	9500	4.0	9500	4.0	9500^{+500}_{-250}	$4.0^{+0.50}_{-0.00}$
TYC-461-622-1	6250	4.5	6000	4.0	6250	4.0	6250^{+000}_{-250}	$4.0^{+0.50}_{-0.00}$
TYC-9329-60-1	6500	4.0	6500	4.0	6500	4.5	6500^{+250}_{-250}	$4.0^{+0.50}_{-0.00}$

Table 2.3: Photometry and distances from the literature, along with the extinction and scaling factor for each target.

Name	B (mag)	V (mag)	R (mag)	D (pc)	A _V mag	D/R _* pc/R _⊙
HIP 22112	8.730	8.442	8.250	603.50 ^{+19.23} _{-19.23}	1.17 ^{+0.06} _{-0.08}	121.6 ^{+5.9} _{-4.3}
HIP 23201	8.635	8.311	8.090	266.40 ^{+4.18} _{-4.18}	1.22 ^{+0.07} _{-0.06}	102.1 ^{+3.8} _{-4.0}
HIP 25763	9.927	9.323	8.910	194.73 ^{+2.38} _{-2.38}	0.43 ^{+0.05} _{-0.06}	79.8 ^{+2.5} _{-2.1}
HIP 28561	6.289	6.350	6.390	266.84 ^{+9.54} _{-9.54}	0.06 ^{+0.05} _{-0.04}	64.2 ^{+1.5} _{-1.8}
HIP 29635	6.557	6.588	6.610	269.63 ^{+4.79} _{-4.79}	0.11 ^{+0.04} _{-0.04}	65.7 ^{+1.6} _{-1.5}
HIP 30448	6.158	6.215	6.260	262.59 ^{+6.78} _{-6.78}	0.07 ^{+0.04} _{-0.06}	60.1 ^{+2.1} _{-1.4}
HIP 38779	6.726	6.729	6.730	673.67 ^{+0.00} _{-0.00}	0.23 ^{+0.04} _{-0.05}	70.7 ^{+2.2} _{-1.6}
HIP 48613	5.709	5.704	5.700	99.34 ^{+0.91} _{-0.91}	0.08 ^{+0.02} _{-0.03}	38.0 ^{+0.7} _{-0.4}
HIP 57027	7.294	6.936	12.650	104.91 ^{+4.15} _{-4.15}	0.00 ^{+0.21} _{-0.00}	41.9 ^{+15.5} _{-8.3}
HIP 57143	7.167	7.122	7.090	422.71 ^{+12.08} _{-12.08}	0.45 ^{+0.05} _{-0.05}	89.5 ^{+2.7} _{-2.7}
HIP 61738 ^{*†}	6.600	6.500	-	174.52 ^{+2.35} _{-2.35}	0.64 ^{+0.00} _{-0.00}	57.3 ^{+0.0} _{-0.0}
HIP 74911 [*]	4.923	5.002	5.000	102.88 ^{+0.00} _{-0.00}	0.08 ^{+0.01} _{-0.00}	34.6 ^{+0.0} _{-0.2}
HIP 77289	7.025	7.070	7.100	389.70 ^{+20.04} _{-20.04}	0.14 ^{+0.04} _{-0.05}	91.3 ^{+2.8} _{-2.1}
HIP 81710	5.795	5.877	5.930	234.31 ^{+4.26} _{-4.26}	0.09 ^{+0.04} _{-0.04}	59.4 ^{+1.5} _{-1.4}
HIP 92364	8.506	8.225	8.050	270.52 ^{+4.08} _{-4.08}	0.98 ^{+0.07} _{-0.08}	91.8 ^{+4.4} _{-3.6}
HIP 94260	7.480	7.394	7.340	265.99 ^{+3.30} _{-3.30}	0.30 ^{+0.03} _{-0.03}	75.0 ^{+1.3} _{-1.4}
TYC-461-622-1	10.340	9.751	9.350	149.63 ^{+1.88} _{-1.88}	0.42 ^{+0.06} _{-0.06}	98.4 ^{+3.2} _{-2.9}
TYC-9329-60-1	10.344	9.832	9.490	272.98 ^{+2.18} _{-2.18}	0.29 ^{+0.03} _{-0.03}	116.8 ^{+2.1} _{-1.9}

(a) * - Distance taken from Hipparcos Catalog [van Leeuwen, 2007], all others are taken from Gaia [Gaia Collaboration, 2018]; † - Photometric data taken from Egret et al. [1992], all other photometric data taken from Zacharias et al. [2004]

Table 2.4: The derived stellar parameters.

Name	T_{eff} (K)	$\log(g)$ (cm/s^2)	D (pc)	A_V (mag)	$\log(L_*)$ [L_\odot]	M_* (M_\odot)	R_* (R_\odot)	Age (Myr)
HIP 22112	14500^{+500}_{-500}	$4.0^{+0.50}_{-0.50}$	$603.50^{+19.23}_{-19.23}$	$1.17^{+0.06}_{-0.08}$	$2.99^{+0.12}_{-0.13}$	$5.04^{+0.01}_{-0.08}$	$4.96^{+0.35}_{-0.38}$	$0.40^{+0.01}_{-0.00}$
HIP 23201	13000^{+500}_{-500}	$4.0^{+0.00}_{-0.50}$	$266.40^{+4.18}_{-4.18}$	$1.22^{+0.07}_{-0.06}$	$2.24^{+0.12}_{-0.11}$	$3.49^{+0.12}_{-0.07}$	$2.61^{+0.15}_{-0.13}$	$1.66^{+0.02}_{-0.03}$
HIP 25763	6250^{+500}_{-250}	$4.5^{+0.50}_{-0.00}$	$194.73^{+2.38}_{-2.38}$	$0.43^{+0.05}_{-0.06}$	$0.91^{+0.17}_{-0.11}$	$1.60^{+0.03}_{-0.02}$	$2.44^{+0.10}_{-0.10}$	$7.44^{+0.24}_{-0.64}$
HIP 28561	11750^{+750}_{-000}	$4.0^{+0.50}_{-0.00}$	$266.84^{+9.54}_{-9.54}$	$0.06^{+0.05}_{-0.04}$	$2.47^{+0.16}_{-0.05}$	$3.99^{+0.02}_{-0.01}$	$4.16^{+0.27}_{-0.24}$	$1.42^{+0.38}_{-0.51}$
HIP 29635	11000^{+500}_{-500}	$3.5^{+0.00}_{-0.00}$	$269.63^{+4.79}_{-4.79}$	$0.11^{+0.04}_{-0.04}$	$2.35^{+0.11}_{-0.11}$	$3.56^{+0.04}_{-0.02}$	$4.10^{+0.17}_{-0.17}$	$1.14^{+0.06}_{-0.03}$
HIP 30448	11750^{+250}_{-250}	$3.5^{+0.50}_{-0.00}$	$262.59^{+6.78}_{-6.78}$	$0.07^{+0.04}_{-0.06}$	$2.51^{+0.08}_{-0.09}$	$4.04^{+0.02}_{-0.01}$	$4.37^{+0.22}_{-0.26}$	$0.87^{+0.02}_{-0.00}$
HIP 38779	11750^{+000}_{-500}	$3.5^{+0.00}_{-0.50}$	$673.67^{+0.00}_{-0.00}$	$0.23^{+0.04}_{-0.05}$	$3.19^{+0.02}_{-0.10}$	$6.73^{+0.13}_{-0.14}$	$9.53^{+0.22}_{-0.29}$	$0.20^{+0.01}_{-0.00}$
HIP 48613	9500^{+500}_{-500}	$4.0^{+0.00}_{-0.50}$	$99.34^{+0.91}_{-0.91}$	$0.08^{+0.02}_{-0.03}$	$1.70^{+0.09}_{-0.12}$	$2.46^{+0.04}_{-0.15}$	$2.61^{+0.05}_{-0.07}$	$3.45^{+0.13}_{-0.06}$
HIP 57027	6750^{+250}_{-250}	$4.5^{+0.50}_{-0.00}$	$104.91^{+4.15}_{-4.15}$	$0.00^{+0.21}_{-0.00}$	$1.07^{+0.29}_{-0.37}$	$1.67^{+0.23}_{-0.18}$	$2.50^{+0.74}_{-0.75}$	$7.39^{+3.68}_{-2.41}$
HIP 57143	14000^{+500}_{-500}	$4.0^{+0.50}_{-0.50}$	$422.71^{+12.08}_{-12.08}$	$0.45^{+0.05}_{-0.05}$	$2.89^{+0.11}_{-0.11}$	$5.03^{+0.02}_{-0.83}$	$4.72^{+0.29}_{-0.27}$	$0.52^{+0.07}_{-0.08}$
HIP 61738	13000^{+500}_{-500}	$4.0^{+0.00}_{-0.00}$	$174.52^{+2.35}_{-2.35}$	$0.64^{+0.00}_{-0.00}$	$2.38^{+0.08}_{-0.08}$	$3.68^{+0.19}_{-0.22}$	$3.05^{+0.04}_{-0.04}$	$1.50^{+0.05}_{-0.30}$
HIP 74911	12000^{+1000}_{-250}	$4.0^{+0.50}_{-0.00}$	$102.88^{+0.00}_{-0.00}$	$0.08^{+0.01}_{-0.00}$	$2.22^{+0.14}_{-0.04}$	$3.32^{+0.23}_{-0.01}$	$2.97^{+0.02}_{-0.00}$	$1.62^{+0.02}_{-0.09}$
HIP 77289	12500^{+500}_{-750}	$3.5^{+0.50}_{-0.50}$	$389.70^{+20.04}_{-20.04}$	$0.14^{+0.04}_{-0.05}$	$2.60^{+0.13}_{-0.18}$	$4.01^{+0.18}_{-0.03}$	$4.27^{+0.33}_{-1.07}$	$0.69^{+0.18}_{-0.01}$
HIP 81710	14000^{+1000}_{-500}	$4.0^{+0.00}_{-0.00}$	$234.31^{+4.26}_{-4.26}$	$0.09^{+0.04}_{-0.04}$	$2.73^{+0.16}_{-0.10}$	$4.10^{+0.34}_{-0.00}$	$3.94^{+0.17}_{-0.17}$	$0.67^{+0.01}_{-0.02}$
HIP 92364	10750^{+250}_{-250}	$3.5^{+0.50}_{-0.00}$	$270.52^{+4.08}_{-4.08}$	$0.98^{+0.07}_{-0.08}$	$2.02^{+0.09}_{-0.10}$	$2.96^{+0.01}_{-0.03}$	$2.95^{+0.17}_{-0.18}$	$2.25^{+0.03}_{-0.02}$
HIP 94260	9500^{+500}_{-250}	$4.0^{+0.50}_{-0.00}$	$265.99^{+3.30}_{-3.30}$	$0.30^{+0.03}_{-0.03}$	$1.97^{+0.12}_{-0.07}$	$2.74^{+0.16}_{-0.00}$	$3.55^{+0.11}_{-0.10}$	$2.14^{+0.02}_{-0.06}$
TYC-461-622-1	6250^{+000}_{-250}	$4.0^{+0.50}_{-0.00}$	$149.63^{+1.88}_{-1.88}$	$0.42^{+0.06}_{-0.06}$	$0.50^{+0.04}_{-0.11}$	$1.23^{+0.01}_{-0.03}$	$1.52^{+0.07}_{-0.06}$	$15.71^{+0.87}_{-0.97}$
TYC-9329-60-1	6500^{+250}_{-250}	$4.0^{+0.50}_{-0.00}$	$272.98^{+2.18}_{-2.18}$	$0.29^{+0.03}_{-0.03}$	$0.94^{+0.08}_{-0.09}$	$1.56^{+0.04}_{-0.02}$	$2.34^{+0.06}_{-0.06}$	$8.50^{+0.17}_{-0.33}$

Chapter 3

Accretion Rate and IR Excess Measurements

3.1 Introduction

Herbig stars are found to be similar to the Classical T Tauri stars (CTTs) by having similar properties like the presence of discs around them, presence of emission lines, both have lower surface gravities than main sequence (MS) stars and both exhibit UV excess. It is known that the Herbig stars are found to have two different types of discs based on the IR excess emitted from the disc [Meeus et al., 2001], as discussed in Chapter 1. Some discs are found to have gaps in them and presence of planets is also observed in the discs (Currie et al. [2014], Close et al. [2014], Quanz et al. [2013], Brittain et al. [2013]). Accretion plays an important role in influencing the mass of the planets formed within the discs as the newly forming planets need to feed on the disc material. Accretion also plays as a source of energy for the emission lines and the UV excess observed in their spectra (Garrison [1978], Donehew and Brittain [2011], Mendigutía et al. [2011]).

Accretion in the CTTs occur through magnetospheric accretion [Calvet and Gullbring, 1998]. The observed UV excess is explained by a theory (Gullbring et al. [1998], Gullbring et al. [2000], Ingleby et al. [2013]), according to which, the magnetic field lines from the central star truncates the material from the inner regions of the disc, which is then funnelled onto the star. The observed emission line are also seen to be a result of accretion (Muzerolle et al. [1998b], Muzerolle et al. [2001], Kurosawa et al. [2011]) and hence can be used to determine the accretion rates. For the magnetospheric accretion to be applicable, the magnetic field lines from the central star must be strong enough to be able to truncate the disc, it is of the order of kilo-Gauss for CTTs (Ghosh and Lamb [1979], Koenigl [1991], Shu et al. [1994], Johns-Krull [2007], Bouvier et al. [2007]). To date studies have found only a few Herbig stars to have magnetic fields (Wade et al. [2005], Catala et al. [2007], Hubrig et al. [2009]). A work carried out by Alecian et al. [2013] showed that only 5 out of 70 Herbig stars were found to have magnetic fields. Though it is unclear if the detected magnetic field is a remnant of the giant molecular cloud from which the star has formed or if it is due to the convective motions of the material within the star [Charbonneau and MacGregor, 2001].

The accretion rates of the stars can also be determined using the emission lines seen in their spectra. It has been found that the accretion luminosity is correlated to the luminosities of the emission lines of the stars (Rigliaco et al. [2012], Herczeg and Hillenbrand [2008], Dahm [2008], Calvet et al. [2004], Muzerolle et al. [1998a]). Details like the motion of the gases and the geometry of the emitting regions can be provided by the various profiles of the spectral lines. For example, the presence of double peaked lines in emission signifies that the disc is rotating (Acke et al. [2005], Acke and van den Ancker [2006], Bagnoli et al. [2010]). Mendigutía et al. [2011] shows that a few luminosity relationships which holds good for CTTs also holds good for Herbig stars. Hence the line profiles can be used to determine the accretion rates of the stars. It is easier to obtain the emission line measurements than to obtain the UV excess measurements to determine the accretion rates (\dot{M}_{acc}), as emission lines at a variety of different wavelengths can be used for measurements.

This section 3.2 of this Chapter deals with determining the accretion rates for the entire sample of 18 Herbig (see Chapter 2) stars by measuring the equivalent widths of the H_α emission line in their spectra. The stellar parameters determined in Chapter 2 are used to calculate \dot{M}_{acc} . The section 3.3 explains measurements of IR excess of the stars.

3.2 Accretion rate Measurements

PMS stars accrete material from their disks for a very long time until the material in the disc is accreted entirely onto the star or removed due to planet formation or photoevaporation. The accretion rates of Herbig Ae stars was found to be about $10^{-9} < \dot{M}_{acc} < 10^{-6} M_\odot/\text{yr}$ [Garcia Lopez et al., 2006]. The accretion rate in most of the Herbig Ae stars are low [Garcia Lopez et al., 2006]. The inner rim of the disc receives direct stellar radiation and a puffed-up rim is formed (Dominik et al. [2003], Benisty et al. [2010], Isella et al. [2008], Dullemond et al. [2001]).

I determined the stellar parameters like T_{eff} , $\log(g)$, A_V , L_* , R_* , M_* and age for the sample of 18 stars, in the previous Chapter. I use these parameters to determine the accretion rates of the stars. In this work, the line profile is used. First, the equivalent width (EW) of the Hydrogen-alpha (H_α) emission line of the Balmer series is determined, from which the line flux is calculated. Using this the line luminosity is determined and then the accretion rate is calculated.

3.2.1 Equivalent Width Measurements

Emission lines contain information about the stars and their environment. The presence of emission particularly at H_α shows that the star is strongly accreting. The strengths of the lines can be used to gain information on the energy imparted due to accretion or heating. Amongst the other lines in the Balmer series H_α is used as it is the lowest transition, from $n=3$ to $n=2$. This is the reason why it is seen as the strongest emission line in the optical spectra of Herbig stars. The presence this emission line was used initially to identify and classify Herbig stars [Herbig, 1960] and has helped detecting many more (Finkenzeller and Mundt [1984], The et al. [1994], Vieira et al. [2003]).

The strength of each observed emission line is calculated by measuring the Equivalent Width (EW) and is shown in the expression below:

$$EW_{obs} = \int_a^b \frac{I_c - I_\lambda}{I_c} \quad (3.1)$$

Where a and b are the blue and red wavelength points respectively, I_c is the continuum intensity and I_λ is the intensity of the line at a particular wavelength. I normalised the line such that the continuum level is at unity. To determine the EW of the H_α emission line of the Balmer series, the spectra of the stars obtained by X-Shooter is used along with the spectra of the Bosz model. To achieve this, I normalised the H_α emission line of the spectra using IRAF based on the continuum region on both the sides. The EW is measured for this normalised line using IRAF and is called as observed equivalent width, EW_{obs} .

Due to the stellar photosphere, there will be some intrinsic absorption of the line in the majority of the observed emission lines of the observed spectra. EW_{obs} is a combination of the intrinsic absorption and true circumstellar emission, and the true emission is stronger than the corrected equivalent width, EW_{cor} . The intrinsic equivalent width must be subtracted from the observed to obtain EW_{corr} . Hence, it is necessary to determine the EW of the intrinsic

absorption line, EW_{int} . This is done using the model spectra.

The strength of the intrinsic absorption line depends on the temperature, surface gravity, and metallicity of the star. These parameters of the stars are already obtained by performing spectral fitting of the spectra obtained using XShooter and the model spectra from Bosz model. The model spectrum corresponding to the temperature obtained for each individual star is used to find EW_{int} . To determine EW_{int} , the H_α absorption line of the spectra is normalised based on the same continuum regions, as chosen for the observed spectra, on either side of the line. The normalisation is done using IRAF and also the EW is measured using the same. Once EW_{obs} and EW_{int} is known, the corrected Equivalent Width, EW_{corr} , is determined using the relation:

$$EW_{corr} = EW_{obs} - EW_{int} \quad (3.2)$$

The line flux, F_{line} , can now be calculated with the known value of EW_{corr} . The expression which relates the line flux with corrected equivalent width is shown below:

$$F_{line} = |EW_{corr}| \times F_\lambda \quad (3.3)$$

Where F_λ is the continuum flux corresponding to the central wavelength of the line. The table 3.1 shows the EW_{corr} , F_λ and F_{line} for all the targets.

The line luminosity, L_{line} , of the emission line can be determined as the distance of the stars are known (shown in table 2.3 with the references). The expression used to calculate L_{line} is:

$$L_{line} = 4\pi D^2 F_{line} \quad (3.4)$$

By now I calculated EW_{obs} , EW_{int} , EW_{corr} , F_λ , F_{line} and L_{line} for all the stars

in the sample, which will now be used to determine the accretion luminosity, L_{acc} , and accretion rate \dot{M}_{acc} of the stars.

Even though many different lines can be used for measuring accretion rates, the most commonly used are H_α , $Pa\beta$, $Br\gamma$ and $[OI]_{\lambda 6300}$, and H_α is used in this work. These lines are frequently used as it is seen that for these lines the luminosity and accretion luminosity are correlated (Muzerolle et al. [1998a], Calvet et al. [2004], Dahm [2008], Herczeg and Hillenbrand [2008], Mendigutía et al. [2011], Rigliaco et al. [2012]). The relationship is shown below:

$$\log\left(\frac{L_{acc}}{L_\odot}\right) = A + B \times \log\left(\frac{L_{line}}{L_\odot}\right) \quad (3.5)$$

Where A and B are constants, which are different for different lines. The values of A and B obtained by [Alcalá et al., 2014] are (1.50 ± 0.26) and (1.12 ± 0.07) respectively. The values of the same constants A and B obtained by [Fairlamb et al., 2017] is (2.09 ± 0.06) and (1.00 ± 0.05) respectively. The values obtained by Fairlamb et al. [2017] is used in this work. This approach of measuring the accretion rates from accretion luminosity is more effective than from UV excess as hot stars with low accretion rates cannot be detected easily by a UV excess.

The accretion rate, \dot{M}_{acc} , can now be calculated using the relation:

$$L_{acc} = \frac{GM_*}{R_*} \dot{M}_{acc} \quad (3.6)$$

Where L_{acc} is the accretion luminosity, G is the gravitational constant, M_* is the mass of the star and R_* is the radius of the star. All these parameters are previously determined in Chapter 2. The accretion rate can be calculated using the values obtained. The table 3.2 shows the obtained accretion rates for the sample.

3.3 Accretion Rate vs Stellar Parameters

The stellar parameters, T_{eff} , $\log(g)$, A_V , L_* , D , M_* , R_* and age of the stars are determined in Chapter 2 and the accretion rates for the entire sample was determined in the previous section of this chapter. In chapter 2, the plot between the age and the temperature of the stars showed that the younger stars are usually hotter than the older stars. In this section, I plot the parameters with the accretion rates to see how each one of them varies with accretion rates.

Figure 3.1 shows how accretion rate varies with age. The stars with mass lower than $1.5 M_\odot$ is shown in blue dots, the stars in the mass range $1.5-3.5 M_\odot$ are shown in orange dots and the stars massive than $3.5 M_\odot$ are shown in green dots. The plot shows us that the younger stars have high accretion rates compared to the older stars. The accretion rate diminishes as the star grows older. This indicates that the accretion rate tells us how the Herbig stars evolve. When the stars are young, the discs around them have more material which is accreted onto the star. Gradually, the material of the disc is lost as it is accreted onto the stars or lost due to photoevaporation or due to planet formation [Gorti and Hollenbach, 2009]. Hence, the accretion rates of the older stars is lower compared to the younger stars.

In this work, the relation to between the accretion rate and age is determines as $\dot{M}_{acc} \propto t^{-2.10 \pm 0.30}$. Fairlamb et al. [2015] determined a fit to the data provides a relationship between the accretion rate and age as $\dot{M}_{acc} \propto t^{-\eta}$, where t is the age in Myr and $\eta = 1.92 \pm 0.09$ [Fairlamb et al., 2015]. This relationship is seen to vary for Herbig Ae (HAes) and Herbig Be (HBes) stars. For HBes, η is found to be 2.02 ± 0.22 , which is similar to the results for all Herbig stars, but HAes was found to have a steeper relationship with $\eta = 4.06 \pm 0.53$ [Fairlamb et al., 2015]. Mendigutía et al. [2012] obtained a more general relationship for all Herbig stars as $\eta = 1.8$. Classical T Tauri stars (CTTs) are also seen to follow a same trend in the relationship between the age and the accretion rates of the stars and η is found to be in the range 1.5-2.8 [Hartmann et al., 1998]. But, recent studies have shown that there is a difference in the relationship $\dot{M}_{acc} \propto t^{-\eta}$ for Herbig stars and CTTs, as the relationship was found to be

shallower, $\dot{M}_{acc} \propto t^{-2}$ (Sicilia-Aguilar et al. [2010]; Caratti o Garatti et al. [2012]). This implies that massive stars have high accretion rates and are only observable at their younger ages as they evolve quicker and the less massive stars have a longer Pre-Main Sequence lifetime.

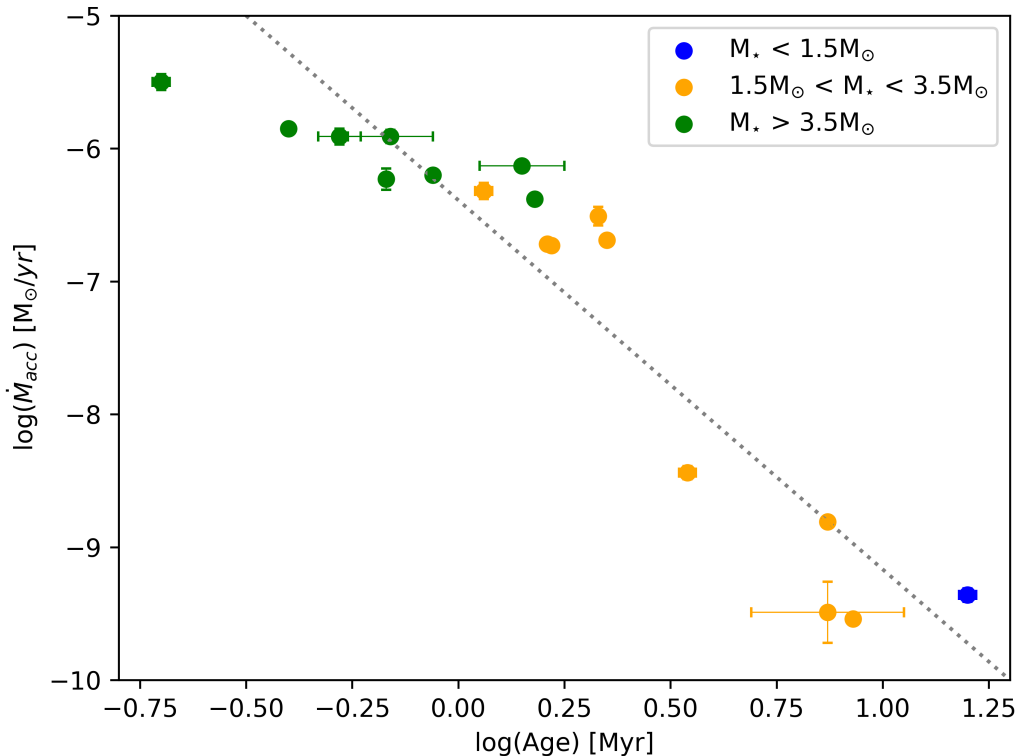


Figure 3.1: The accretion rates of the stars are plotted against their ages; stars with mass lower than $1.5 M_{\odot}$ are shown in blue dots, stars in the mass range 1.5 - $3.5 M_{\odot}$ are shown in orange dots and those with mass greater than $3.5 M_{\odot}$ are shown in green dots.

Figure 3.2 shows the plot of T_{eff} and \dot{M}_{acc} of the stars, obtained in Chapters 2 and 3, respectively. The stars in the different mass ranges are shown in different colored dots. It is clearly seen that the accretion rate increases steadily with an increase in the temperature. It is seen that the stars massive than $3.5 M_{\odot}$ are seen to have higher temperatures as well as higher accretion rates when compared to lower mass stars which are found to have lower temperatures and lower accretion rates. CTTs are also seen to follow a similar relationship between the temperature and accretion rates of the stars [Hartmann et al., 1998].

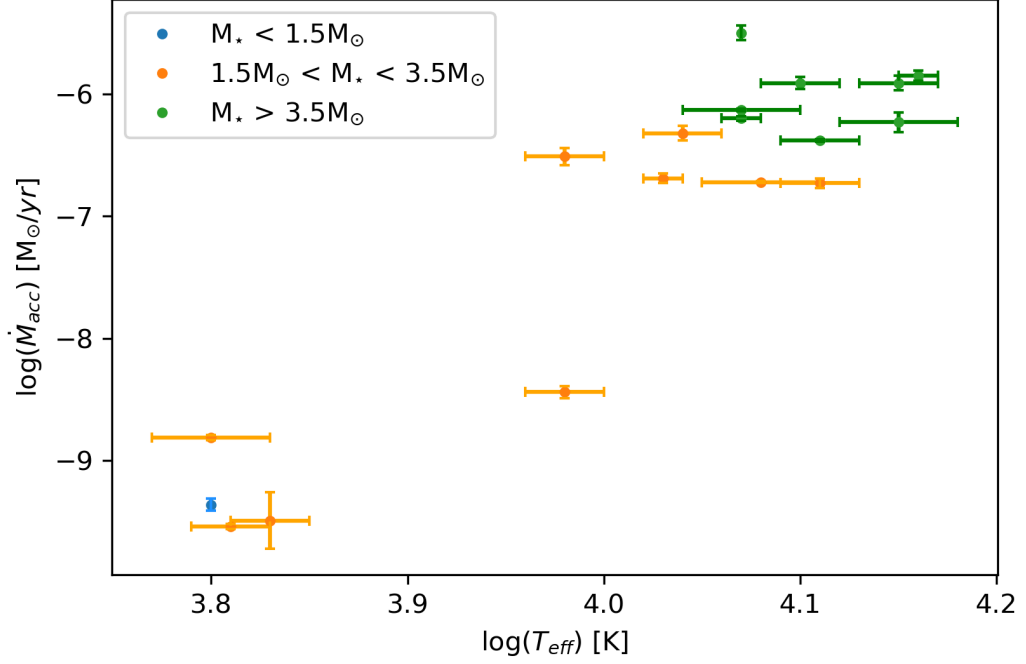


Figure 3.2: Plot showing \dot{M}_{acc} against T_{eff} , where stars in different mass groups are shown in different colors: blue dots for stars with mass lesser than $1.5 M_{\odot}$, orange dots for stars in the mass range $1.5-3.5 M_{\odot}$ and green dots for stars with masses greater than $3.5 M_{\odot}$.

Fig 3.3 shows the plot of the stellar mass and accretion rates determined in Chapters 2 and 3, respectively. The stars in different age groups are shown in different colored dots: the stars younger than 5 Myr are represented by blue dots and stars older than 5 Myr are represented by orange dots. It is seen that the older stars are seen to have lower accretion rates compared to the younger stars. Fig 3.4 shows the plot of the stellar mass and accretion rates where the stars are grouped based on their masses.

In this work, I obtained the relation as $\dot{M}_{acc} \propto M_*^{7.69 \pm 0.50}$. Fairlamb et al. [2015] obtained that for HAes the best fit of M_* and \dot{M}_{acc} is shown to be $\dot{M}_{acc} \propto M_*^{8.42 \pm 1.37}$ and HBes have a shallower relationship, $\dot{M}_{acc} \propto M_*^{2.82 \pm 0.39}$. In general, for all Herbig stars, the relationship is seen to be $\dot{M}_{acc} \propto M_*^{2.0 \pm 0.2}$ (Muzerolle et al. [2005]; Natta et al. [2006]). Herbig stars have higher accretion rates than CTTs and a steeper relationship than CTTs is observed between the accretion rate and stellar mass for Herbig stars. This might be because

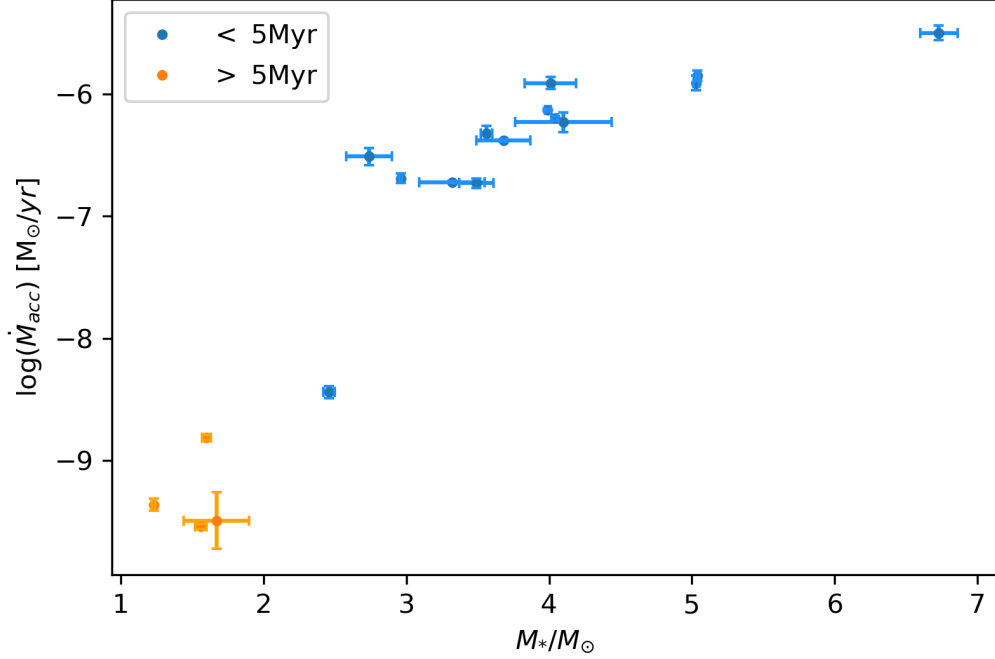


Figure 3.3: Plot of accretion rates against the mass of the stars, where the stars younger than 5 Myr are shown in blue dots and the older stars are shown in orange dots.

Herbig stars are in the early stages of accretion. The relationship for CTTs is shallower: $M_* \propto \dot{M}_{acc}^{2.0}$ [Tilling et al., 2008].

Fig. 3.5 shows the plot of the stellar luminosity and accretion luminosity. The stars in the different mass ranges are shown in different colored dots. The stars with mass lower than $1.5M_\odot$ is shown in blue dots, the stars in the mass range $1.5\text{--}3.5 M_\odot$ are shown in orange dots and the stars with mass greater than $3.5 M_\odot$ are shown in green dots. By definition, massive stars have greater stellar luminosities and the massive stars in this work follow that and also they are seen to have greater accretion luminosities compared to the lower mass stars.

In this work, the relation between the luminosity of the star and the accretion luminosity is obtained as $L_{acc} \propto L_*^{1.43 \pm 0.45}$. Fairlamb et al. [2015] determined the best fit to be $L_{acc} \propto L_*^{1.07 \pm 0.06}$. This is in agreement with Mendigutía et al. [2011], where they found $L_{acc} \propto L_*^{1.2}$ for Herbig stars. Like earlier comparisons, HAes are seen to have a relationship $L_{acc} \propto L_*^{1.53 \pm 0.14}$ and HBes have

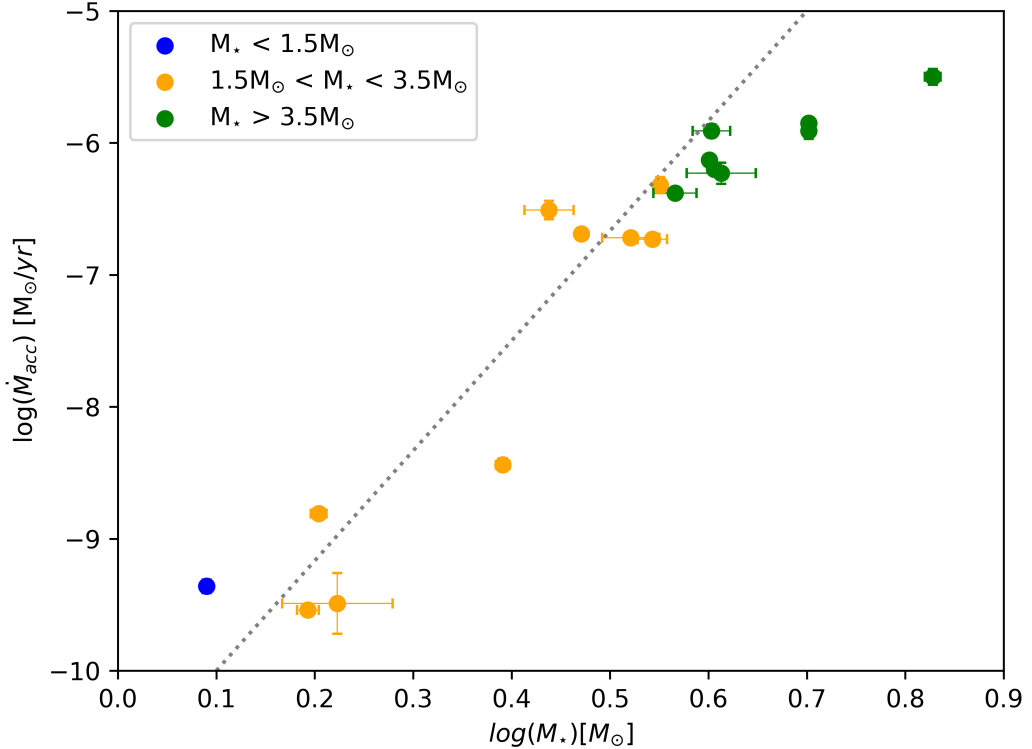


Figure 3.4: Plot of accretion rates against the mass of the stars, where stars in different mass groups are shown in different colors: blue dots for stars with mass lesser than $1.5 M_{\odot}$, orange dots for stars in the mass range $1.5-3.5 M_{\odot}$ and green dots for stars with masses greater than $3.5 M_{\odot}$.

a shallower relationship, as seen in the other comparisons, $L_{acc} \propto L_*^{0.84 \pm 0.13}$. CTTs also follow a similar trend, where, $L_{acc} \propto L_*^{1.5}$ (Natta et al. [2006]; Tilling et al. [2008]). These relationships that were obtained suggests that stellar luminosity and the accretion luminosity are tightly correlated, but the exact relationship changes in exponent as the stars cross into the HBe regime.

The relationships studied indicate that the accretion rate is an evolutionary property of the Herbig stars. The accretion rate decreases as the star approaches the Main-Sequence, and this is might be due to the loss of the material in the disc around them due to accretion onto the star, photoevaporation or planet formation. Discs dispersal explained in the context of photoevaporation suggests that the lifetimes of the discs are shorter for high mass stars [Gorti and Hollenbach, 2009]. This explains that the HAes have a steeper

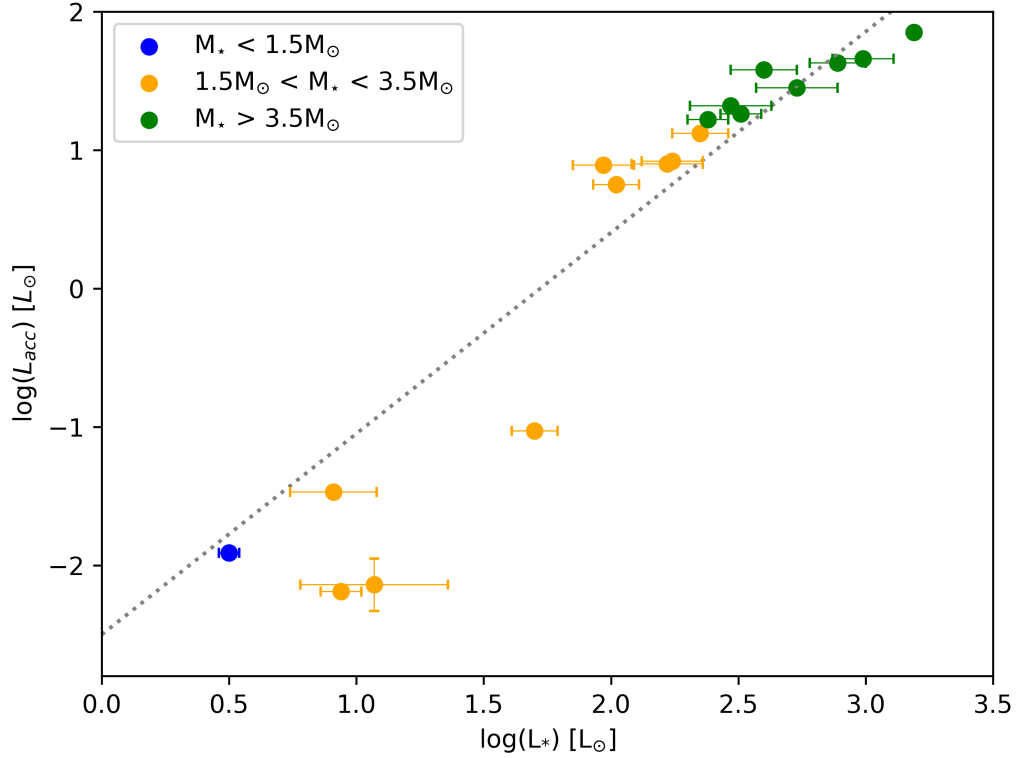


Figure 3.5: The accretion luminosities are plotted against the stellar luminosities, where the stars in different mass ranges are shown in different colors: stars with mass lower than $1.5 M_{\odot}$ are shown in blue, stars in the mass range $1.5-3.5 M_{\odot}$ are shown in orange and those greater than $3.5 M_{\odot}$ are shown in green.

relationship, compared to HBes, as we could be observing the transition stage of disc dispersion as the star approaches the main sequence, resulting in a decreased accretion rate, while HBes have a shallower relationship as they are always younger and might not have existed long enough for the disc dispersal to happen. This makes them similar to CTTs.

3.4 IR Excess Measurements

Studying the IR excess provides a better understanding of the presence and distribution of dust in the disk around the star [Roessiger, 1977]. The observed spectra are a result of the four different combinations: the young star's photosphere, IR excess from the disk around the star, energy emitted in the IR during the accretion process and the interstellar extinction (A_V , which is computed in the second chapter for each star) [Prato et al., 2002]. Every star radiates in the IR, but an excess emission signals the presence of a dust around the star. For stars with strong emission, free-free and bound-free emission might also contribute to the spectra. On the other hand, for absorption-line objects the contribution from the free-free and bound-free emission to the spectra is negligible. Thus, these processes are not taken into account while considering the probable contributions to the observed spectra [Prato et al., 2002].

In this work, I have used the ratio of the dereddened observed flux and the photospheric flux at K-band, at $\lambda = 2.2 \mu\text{m}$, to determine the IR excess.

$$IR_{excess} = \frac{Dereddened\ Observed\ Flux}{Photospheric\ Flux} \quad (3.7)$$

The photospheric flux is the photospheric emission of the star. It is obtained from the BOSZ model spectra for particular stellar effective temperatures of the stars, which is derived in Chapter 2. The K-band magnitude of the stars (shown in table 3.3) is taken from the 2MASS All-Sky Point Source Catalog (PSC) [van Dyk, 2000] and it is used to derive an observed flux which is then dereddened using the extinction derived in Chapter 2; this is the dereddened observed flux. The ratio of the dereddened observed flux and the photospheric flux is calculated as the IR excess at K-band.

Table 3.3 shows the values of the observed flux from the target spectra, the photospheric flux from the BOSZ model at K-band along with the excess obtained. It is seen that the excess obtained varies for each star. I will now

discuss how the IR excess varies with age and accretion rates of the stars.

Figure 3.6 shows the plot between the age of the stars and the IR excess obtained. The stars in the mass range $1.5-3.5 M_{\odot}$ are represented by blue dots and the stars above $3.5 M_{\odot}$ are represented by orange dots. It is seen that there is no steady relationship between the age and the IR excess for our sample.

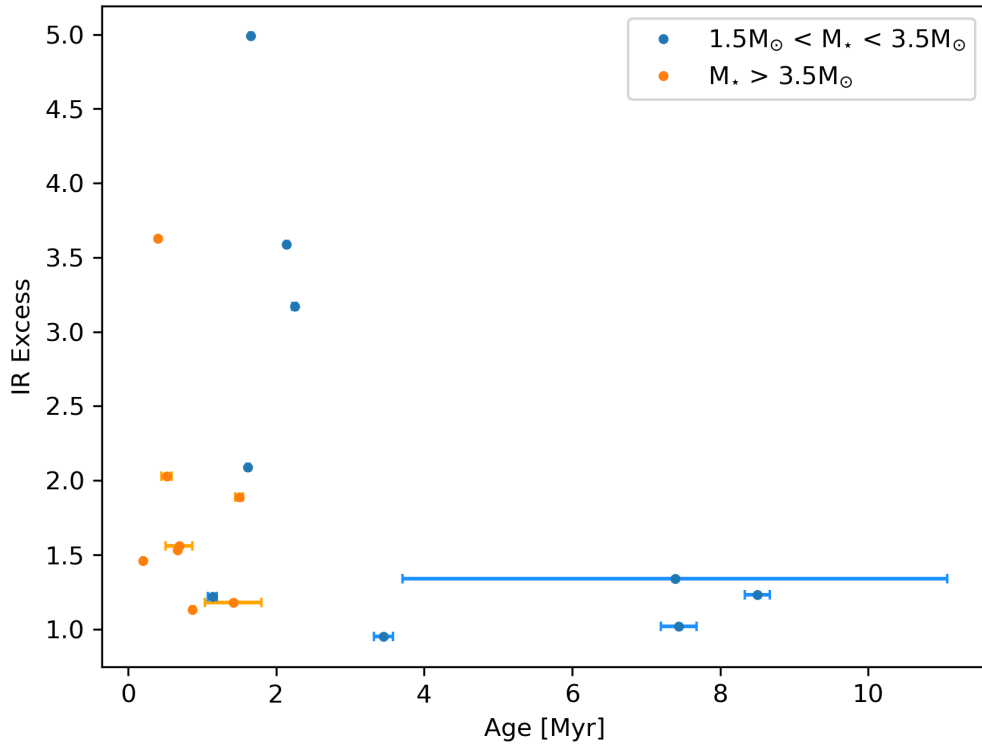


Figure 3.6: The figure represents the plot between age and IR excesses of the stars, where stars in different mass ranges are shown in different colors: blue dots represent stars in the range of $1.5-3.5 M_{\odot}$ and orange dots represent stars with mass greater than $3.5 M_{\odot}$.

Almost all the stars of all age groups are seen to have excesses in the range of 0-2.2, but a few stars with an age of about 2Myr are seen to have higher excesses. It is seen that all stars with their mass greater than $3.5 M_{\odot}$ have excesses in the range of 0-1.5, but a few lower mass stars in the range of $1.5-3.5 M_{\odot}$ are seen to have higher excesses than the 0-1.5 range. Younger stars have more material present in the discs around them as the stars are still accreting, compared to the older stars. This is because the material in the discs around the older stars might be lost due to photoevaporation or due to accretion onto the star or due to the planet formation [Gorti and Hollenbach, 2009]. This tells us that the the younger stars will have more dust than the older stars and can have higher excesses than the older stars. But in this work that trend is not followed and a few older stars have higher excesses compared to the younger ones.

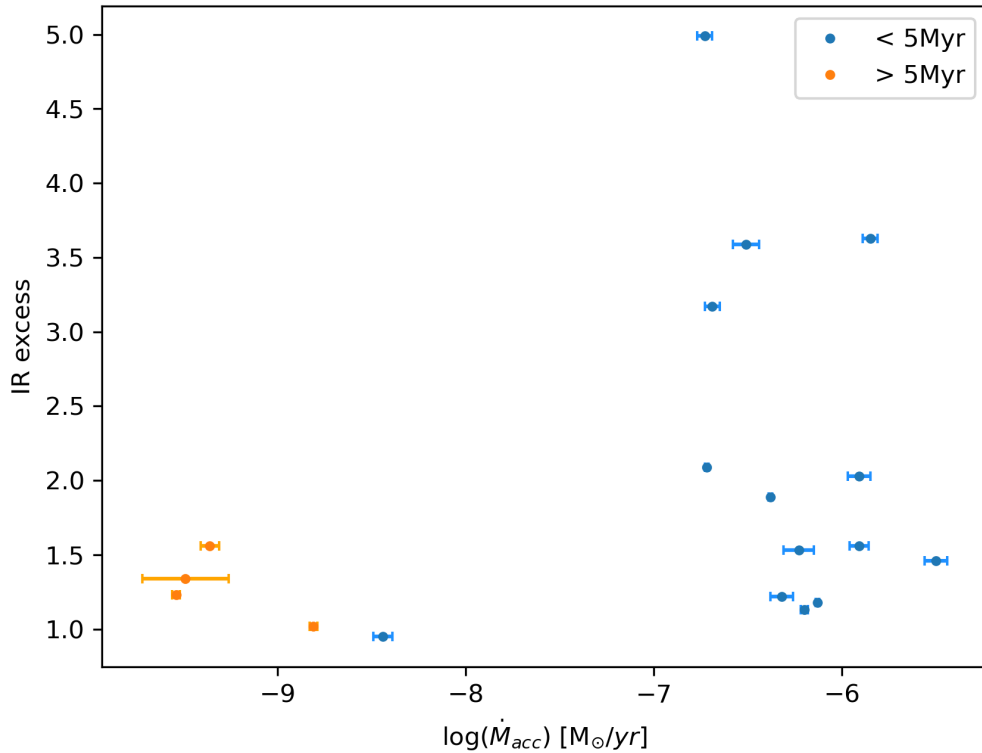


Figure 3.7: The figure represents the plot between the accretion rates and IR excesses of the stars, where stars younger than 5 Myr are represented by blue dots and stars older than 5 Myr are represented by orange dots.

Figure 3.7 shows the accretion rates of the stars plotted against the IR excesses obtained. The stars younger than 5 Myr are represented in blue dots and the stars older than 5 Myr are represented in orange dots. It is seen that younger stars have higher accretion rates compared to the older stars. There is no clear relationship between the IR excess and the accretion rates in the sample of this work, but low accretors all have relatively lower IR excesses while there is a spread for high accretors. The lack of trend is not entirely unexpected because IR traces the dust and the accretion traces the gas around the stars and the stars can have variable accretion rates with time. Hence, a generalised relationship between the accretion rates and the IR excesses cannot be obtained for the targets in this sample.

Table 3.1: Equivalent width (EW) measurements of the H $_{\alpha}$ line for all targets.

Name	EW_{obs} (Å)	EW_{int} (Å)	EW_{corr} (Å)	F$_{\lambda}$ (W m ⁻² Å ⁻¹)	F_{line} (W m ⁻²)
HIP 22112	-9.14 ±0.14	4.74 ±0.35	-13.88 ±0.40	2.37 (±0.20) E-15	3.29 (±0.27) E-14
HIP 23201	-4.76 ±0.20	6.06 ±0.18	-10.82 ±0.23	2.82 (±0.22) E-15	3.05 (±0.24) E-14
HIP 25763	3.61 ±0.08	3.30 ±0.07	0.31 ±0.10	7.52 (±0.43) E-16	2.33 (±0.14) E-16
HIP 28561	-6.07 ±0.90	6.61 ±0.81	-12.68 ±0.97	5.98 (±0.31) E-15	7.58 (±0.39) E-14
HIP 29635	-4.48 ±0.11	4.79 ±0.15	-9.27 ±0.16	5.09 (±0.24) E-15	4.72 (±0.22) E-14
HIP 30448	-5.70 ±0.21	4.34 ±0.17	-10.04 ±0.27	6.85 (±0.39) E-15	6.88 (±0.40) E-14
HIP 38779	-3.82 ±0.06	4.34 ±0.12	-8.16 ±0.17	4.95 (±0.26) E-15	4.04 (±0.22) E-14
HIP 48613	8.20 ±0.2	7.98 ±0.9	0.22 ±0.05	1.14 (±0.04) E-14	2.47 (±0.07) E-15
HIP 57027	3.85 ±0.10	3.90 ±0.11	-0.05 ±0.15	3.44 (±2.26) E-15	1.72 (±0.88) E-16
HIP 57143	-11.40 ±1.1	3.69 ±0.86	-15.09 ±1.35	4.12 (±0.24) E-15	6.22 (±0.38) E-14
HIP 61738	-12.22 ±0.77	4.10 ±0.96	-16.32 ±1.21	8.95 (±0.00) E-15	1.46 (±0.00) E-13
HIP 74911	-4.56 ±1.09	4.57 ±0.65	-9.13 ±0.96	2.13 (±0.02) E-14	1.95 (±0.01) E-13
HIP 77289	-15.57 ±0.23	3.93 ±0.36	-19.50 ±0.58	3.33 (±0.18) E-15	6.49 (±0.34) E-14
HIP 81710	-10.63 ±0.08	3.69 ±0.56	-14.32 ±0.87	9.36 (±0.46) E-15	1.34 (±0.06) E-13
HIP 92364	-3.22 ±0.89	4.91 ±0.36	-8.12 ±0.77	2.48 (±0.22) E-15	2.02 (±0.18) E-14
HIP 94260	-1.82 ±1.20	7.98 ±1.68	-9.80 ±1.09	2.94 (±0.10) E-15	2.88 (±0.10) E-14
TYC-461-622-1	3.03 ±0.30	3.32 ±0.35	-0.29 ±0.50	4.97 (±0.30) E-16	1.43 (±0.09) E-16
TYC-9329-60-1	3.58 ±0.90	3.64 ±0.45	-0.06 ±0.87	3.97 (±0.14) E-16	2.24 (±0.08) E-17

Table 3.2: Table showing the corrected equivalent width, line luminosity, accretion luminosity and accretion rates of all the targets.

Name	EW_{corr} (Å)	$\log(L_{line})$ (L_{\odot})	$\log(L_{acc})$ (L_{\odot})	$\log(\dot{M}_{acc})$ [M_{\odot}/yr]
HIP 22112	-13.88 ± 0.40	$-0.43^{+0.03}_{-0.04}$	$1.66^{+0.03}_{-0.04}$	$-5.85^{+0.04}_{-0.08}$
HIP 23201	-10.82 ± 0.23	$-1.17^{+0.03}_{-0.03}$	$0.92^{+0.04}_{-0.03}$	$-6.73^{+0.04}_{-0.04}$
HIP 25763	0.31 ± 0.10	$-3.56^{+0.02}_{-0.03}$	$-1.47^{+0.02}_{-0.03}$	$-8.81^{+0.02}_{-0.04}$
HIP 28561	-12.68 ± 0.97	$-0.77^{+0.02}_{-0.02}$	$1.32^{+0.02}_{-0.02}$	$-6.13^{+0.01}_{-0.08}$
HIP 29635	-9.27 ± 0.16	$-0.97^{+0.02}_{-0.02}$	$1.12^{+0.02}_{-0.02}$	$-6.32^{+0.06}_{-0.03}$
HIP 30448	-10.04 ± 0.27	$-0.83^{+0.02}_{-0.03}$	$1.26^{+0.02}_{-0.03}$	$-6.20^{+0.02}_{-0.05}$
HIP 38779	-8.16 ± 0.17	$-0.24^{+0.02}_{-0.03}$	$1.85^{+0.02}_{-0.03}$	$-5.50^{+0.06}_{-0.02}$
HIP 48613	0.22 ± 0.05	$-3.12^{+0.01}_{-0.02}$	$-1.03^{+0.01}_{-0.02}$	$-8.44^{+0.05}_{-0.11}$
HIP 57027	-0.05 ± 0.15	$-4.23^{+0.19}_{-0.27}$	$-2.14^{+0.19}_{-0.27}$	$-9.49^{+0.23}_{-0.35}$
HIP 57143	-15.09 ± 1.35	$-0.46^{+0.03}_{-0.02}$	$1.63^{+0.03}_{-0.02}$	$-5.91^{+0.06}_{-0.09}$
HIP 61738	-16.32 ± 1.21	$-0.86^{+0.00}_{-0.00}$	$1.22^{+0.00}_{-0.00}$	$-6.38^{+0.01}_{-0.04}$
HIP 74911	-9.13 ± 0.96	$-1.19^{+0.01}_{-0.00}$	$0.90^{+0.01}_{-0.00}$	$-6.72^{+0.01}_{-0.04}$
HIP 77289	-19.50 ± 0.58	$-0.51^{+0.02}_{-0.03}$	$1.58^{+0.02}_{-0.03}$	$-5.91^{+0.05}_{-0.10}$
HIP 81710	-14.32 ± 0.87	$-0.64^{+0.02}_{-0.02}$	$1.45^{+0.02}_{-0.02}$	$-6.23^{+0.08}_{-0.04}$
HIP 92364	-8.12 ± 0.77	$-1.34^{+0.03}_{-0.04}$	$0.75^{+0.03}_{-0.04}$	$-6.69^{+0.04}_{-0.03}$
HIP 94260	-9.80 ± 1.09	$-1.20^{+0.02}_{-0.01}$	$0.89^{+0.02}_{-0.01}$	$-6.51^{+0.07}_{-0.04}$
TYC-461-622-1	-0.29 ± 0.50	$-3.99^{+0.03}_{-0.03}$	$-1.91^{+0.03}_{-0.03}$	$-9.36^{+0.05}_{-0.04}$
TYC-9329-60-1	-0.06 ± 0.87	$-4.28^{+0.01}_{-0.02}$	$-2.19^{+0.01}_{-0.02}$	$-9.54^{+0.02}_{-0.03}$

Table 3.3: IR Excess measurement at K-Band for all the targets.

Name	K-band magnitude (mag)	Dereddened Observed Flux (W m ⁻² Å ⁻¹)	Photospheric Flux (W m ⁻² Å ⁻¹)	IR Excess
HIP 22112	7.432	1.20 E-16	3.31 E-17	3.63
HIP 23201	6.878	2.10 E-16	4.20 E-17	4.99
HIP 25763	8.063	3.40 E-17	3.32 E-17	1.02
HIP 28561	6.392	1.13 E-16	9.53 E-17	1.18
HIP 29635	6.529	1.04 E-16	8.50 E-17	1.22
HIP 30448	6.307	1.23 E-16	1.09 E-16	1.13
HIP 38779	6.534	1.16 E-16	7.90 E-17	1.46
HIP 48613	5.737	2.10 E-16	2.20 E-16	0.95
HIP 57027	5.847	1.76 E-16	1.31 E-16	1.34
HIP 57143	6.720	1.19 E-16	5.89 E-17	2.03
HIP 61738	6.102	2.51 E-16	1.33 E-16	1.89
HIP 74911	4.428	7.01 E-16	3.36 E-16	2.09
HIP 77289	6.860	7.88 E-17	5.06 E-17	1.56
HIP 81710	5.771	2.05 E-16	1.34 E-16	1.53
HIP 92364	7.118	1.35 E-16	4.25 E-17	3.17
HIP 94260	5.995	2.03 E-16	5.64 E-17	3.59
TYC-461-622-1	8.055	3.39 E-17	2.18 E-17	1.56
TYC-9329-60-1	8.512	1.98 E-17	1.61 E-17	1.23

Chapter 4

Discussion

The stellar parameters like effective temperature, surface gravity, extinction, luminosity, mass, radius and age of 18 Herbig stars were determined using a homogeneous approach which is discussed in Chapter 2. Using these stellar parameters and by measuring the equivalent widths of the H_α emission line, the accretion rates of the stars were determined. The IR spectral index was determined to measure the IR excess of the stars in Chapter 3. I will now include the literature results of additional 4 stars for which the parameters and accretion rates were determined in a similar fashion. I will complement my results with the results obtained for another sample of intermediate-mass stars [Fairlamb et al., 2015] where the same type of observations and analysis methods were used. 4 stars in the mass range 1.5-3.5 M_\odot in my sample are younger than 5 Myr and 31 stars in the same mass range are younger than 5 Myr from Fairlamb et al. [2015], but I also compare to stars older than 5 Myr (5 in my sample and 32 in Fairlamb et al. [2015] sample).

4.1 Additional Targets

27 targets were excluded in the beginning as they were already in the archive. Their parameters are determined and accretion rates measured from the data obtained using XShooter. Among the 27, I found 4 stars for which the parameters for those stars were determined by following a homogeneous method similar to that followed in this work. They are included to the list of the 18 Herbig stars which were studied in the previous chapters to provide a broader understanding.

Table 4.1 shows the list of the stars with their parameters: T_{eff} , $\log(g)$, A_V , L_\odot , M_\odot , R_\odot , D , Age, and line diagnostics like $\log(L_{line})$, $\log(L_{acc})$ and accretion rate $\log(\dot{M}_{acc})$. The stars were chosen from different literature sources. HIP 56379, HIP 78092, HIP 87819 were taken from Fairlamb et al. [2015] and HIP 85755 was taken from Mendigutía et al. [2011]. Fairlamb et al. [2015] used the data from XShooter and followed the method used by Montesinos et al. [2009] and determined the accretion rates using the equivalent width of the Hydrogen alpha, H_α , emission line of the Balmer series. Mendigutía et al. [2011] chose the stars and considered the parameters determined by Montesinos et al. [2009], and determined the equivalent width of H_α , which was used to determine the accretion rate.

4.2 Discussion

I determined the accretion rates for the entire sample in this work in Chapter 3. In this section I will be comparing the results obtained in this work with the previous detections in Herbig stars in literature. Since our criteria of choosing the stars was that they are younger than 5Myr and in the mass range 1.5-3.5 M_\odot , the stars satisfying the similar criteria are chosen from Fairlamb et al. [2015] to compare with the stars in this work. Fairlamb et al. [2015] is chosen to do the comparison as the same methods that are used in this work are used to determine the parameters as well as the accretion rates for the sample in

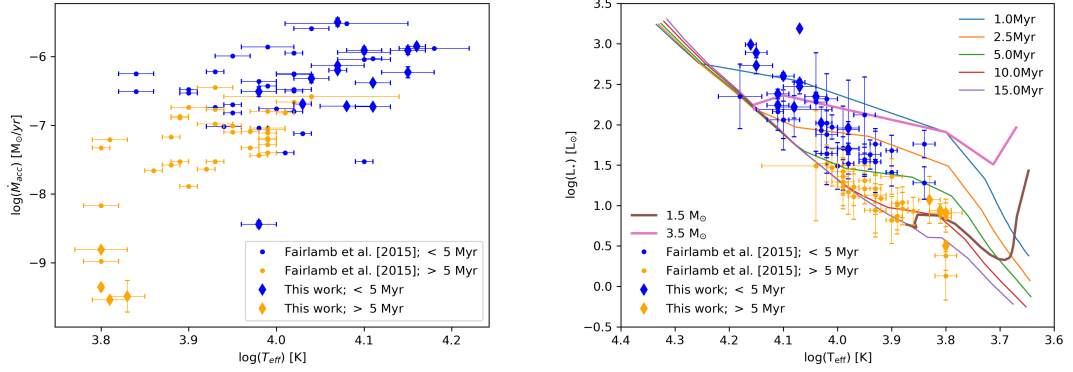


Figure 4.1: The first figure shows T_{eff} vs \dot{M}_{acc} for each target of the sample in this work compared with the values obtained for a selected sample from Fairlamb et al. [2015]; the second figure shows the same targets placed on the HR Diagram with isochrones and evolutionary tracks; The stars younger than 5Myr are shown in blue color and the stars older than 5Myr are shown in orange color.

their work. They worked on a sample of 91 Herbig stars across all mass range and ages to provide a spectroscopic survey of the Herbig stars. They chose 51 stars from The et al. [1994] and 40 from Vieira et al. [2003]. From their sample of 91 stars, I have chosen the stars which fall in mass range $1.5-3.5 M_{\odot}$. I have separated the chosen sample into two categories based on their ages, one being younger than 5 Myr (36 stars) and the other being older than 5 Myr (37 stars). To this selected sample from Fairlamb et al. [2015], I have included the stars which fall in the same two categories to make comparisons. They used the Balmer excess to determine the accretion rates, but provided the measurements of the H_{α} line, such as equivalent widths and line flux in their work, using which I calculated the accretion rates for the selected sample from Fairlamb et al. [2015], as I used the same method in this work to calculate the accretion rates for the entire sample. They determined that the accretion rates were in the order of $10^{-5} - 10^7 M_{\odot}/\text{yr}$ for stars younger than 5 Myr and in the order of $10^7 - 10^9 M_{\odot}/\text{yr}$ for stars older than 5 Myr, and obtained the results that the accretion rate decreases as the stars grow older and approach the main sequence. The accretion rates are plotted against stellar parameters like T_{eff} , M_* and L_* of the stars to compare our sample to the trends established in the aforementioned work.

Figure 4.1 shows the plot between the accretion rate (\dot{M}_{acc}) of the stars versus the effective temperature, T_{eff} . T_{eff} was obtained in Chapter 2 and \dot{M}_{acc} was determined in Chapter 3 of this thesis, combined with the values obtained for the selected sample from Fairlamb et al. [2015] and stars placed on the HR Diagram. As explained in the previous paragraph, the stars are divided into two categories of stars younger and older than 5 Myr. The stars younger than 5 Myr are shown in blue dots and the stars older than 5 Myr are shown in orange dots. It is seen that younger stars in the sample of this work have higher temperatures and the young stars are seen to have higher accretion rates when compared to the older stars. The young stars tend to be more massive in my sample and hence are hotter. In general, young stars accrete more compared to the older stars, implying that \dot{M}_{acc} increases with temperature.

In this work, for Herbig stars with temperature 10000K and lower, the accretion rate is in the range of 10^{-9} and $10^{-10} M_{\odot}/\text{yr}$. For stars with T_{eff} above 10000K, \dot{M}_{acc} is in the range 10^{-6} - $10^{-8} M_{\odot}/\text{yr}$. The Fairlamb et al. [2015] sample has its values of accretion rates very similar to the values obtained in this work. According to the results obtained by Fairlamb et al. [2015], for the stars with effective temperature less than 10000K, \dot{M}_{acc} is in the range 10^{-6} to $10^{-10} M_{\odot}/\text{yr}$ and for stars hotter than 10000K, \dot{M}_{acc} is higher than $10^{-7} M_{\odot}/\text{yr}$. The small variations in the values of \dot{M}_{acc} obtained by Fairlamb et al. [2015] and the results obtained in this work might be due to the sources of the chosen distance or photometry, or because of the different models used to compute the effective temperature and surface gravity [Fairlamb et al., 2015].

Figure 4.2 shows the the plot between the stellar mass and the accretion rates obtained in the Chapters 2 and 3, respectively, along with the selected stars which are included from Fairlamb et al. [2015]; the criteria of selection is explained at the beginning of this section. The stars are color coded based on their ages, blue dots showing the younger stars (< 5 Myr) and the oranges ones showing the older stars (> 5 Myr). It is clearly seen that younger stars have higher accretion rates compared to the older stars which are found to have lower accretion rates. The younger stars are seen to have their accretion rates in the range of $10^{-5} - 10^{-8} M_{\odot}/\text{yr}$ and the older stars have accretion

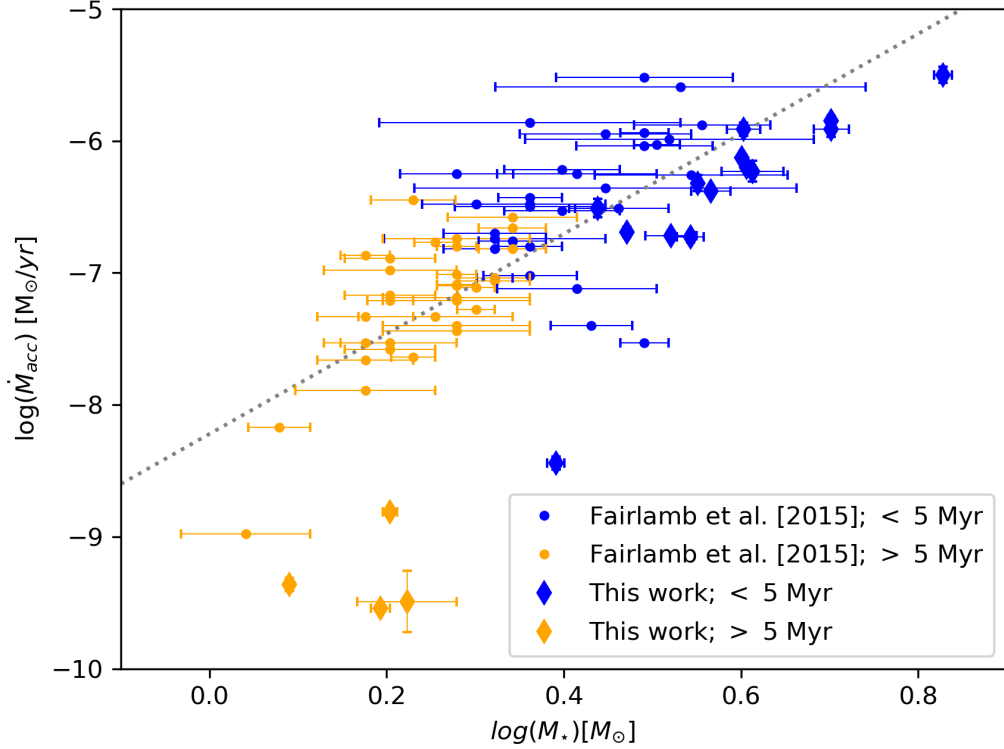


Figure 4.2: The figure shows $\log(M_*)$ vs $\log(\dot{M}_{acc})$ for each target of the sample in this work compared with the values obtained for a selected sample from Fairlamb et al. [2015]. The stars younger than 5Myr are shown in blue color and the stars older than that are shown in orange color.

rates in the range of $10^{-7} - 10^{-9} M_{\odot}/\text{yr}$. Fairlamb et al. [2015] also obtained similar results, where the accretion rates of younger stars (< 5 Myr) were in the range of $10^{-5} - 10^{-7} M_{\odot}/\text{yr}$ and that of older stars (> 5 Myr) were in the range of $10^{-7} - 10^{-9} M_{\odot}/\text{yr}$. Though, a few young and old stars are found to have similar accretion rates: $10^{-7} M_{\odot}/\text{yr}$. The best fit obtained gives $\dot{M}_{acc} \propto M_*^{3.2 \pm 0.60}$. Fairlamb et al. [2015] obtained the relation as $\dot{M}_{acc} \propto M_*^{2.47 \pm 0.70}$ for the plot where he compared the values he obtained with the values obtained in the literature.

As seen in the plot, there are no targets in the right half of the plot, as the targets under consideration fall in the mass range: $1.5-3.5 M_{\odot}$. To compare with the literature results considered, they also obtained similar results. The main result explains that the stars younger than 5 Myr have higher accretion

rates compared to the older stars which are found to have lower accretion rates.

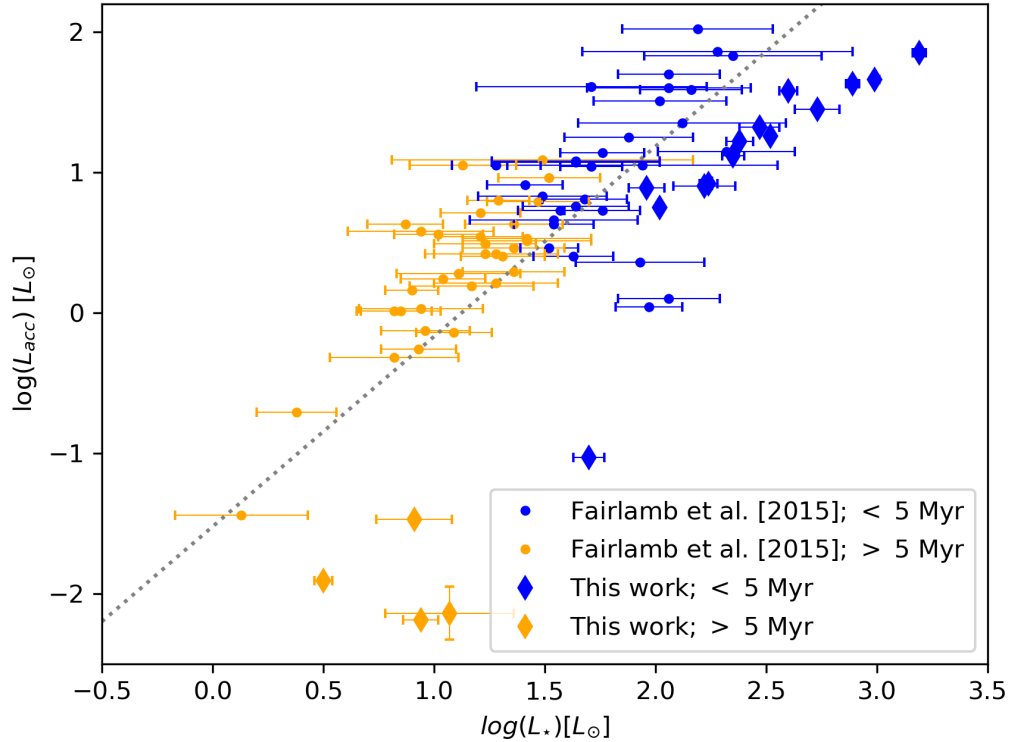


Figure 4.3: The figure shows $\log(L_*)$ vs $\log(L_{acc})$ for each target of the sample in this work compared with the values obtained for a selected sample from Fairlamb et al. [2015]. The stars younger than 5Myr are shown in blue color and the stars older than that are shown in orange color.

Figure 4.3 shows a plot of the stellar luminosity against the accretion luminosity, both determined in the Chapter 3, along with the values obtained for the selected sample from Fairlamb et al. [2015]. The stars younger than 5 Myr are represented in blue dots and the stars older than 5 Myr are represented in orange dots.

It is seen that the younger stars are found to have higher stellar luminosity and accretion luminosity than the older stars. In this work I obtained that the stars younger than 5 Myr had the luminosities in the range of 50-1500 L_\odot and the accretion luminosities in the range of 5-45 L_\odot and the older stars had their luminosities less than 10 L_\odot and the accretion luminosities of about less than

0.10 L_{\odot} . When comparing with the results obtained for the selected sample from Fairlamb et al. [2015], it was seen that the stars younger than 5 Myr had their luminosities in the range of 15-165 L_{\odot} and their accretion luminosities in the range of 1-40 L_{\odot} . The older stars were seen to have luminosities 8-15 L_{\odot} and the accretion luminosities in the range of 0.1-7 L_{\odot} . The best fit obtained gives $L_{acc} \propto L_*^{1.25 \pm 0.10}$. Fairlamb et al. [2015] determined the relation as $L_{acc} \propto L_*^{1.13 \pm 0.03}$ for the plot where he compared the values he obtained with the values obtained in the literature.

In general, the values obtained in this work seen to agree with the values obtained in previous literature of stars in the same mass range. The accretion rates in this work are seen to increase with both temperature and luminosity, which is similar to that seen in literature. In addition, accretion rate is greater for massive stars and it decreases as the star approaches the main sequence. The young stars in this sample tend to be more massive and accrete more as they are young.

Table 4.1: The stellar parameters for the stars in the literature.

Name	T_{eff} (K)	log(g) (cm/s ²)	D (pc)	A_V (mag)	log(L_★) [L _☉]	M_★ (M _☉)	R_★ (R _☉)	Age (Myr)	log(L_{line}) (L _☉)	log(L_{acc}) (L _☉)	log(\dot{M}_{acc}) [M _☉ /yr]
HIP 56379	9750 ⁺⁵⁰⁰ ₋₅₀₀	4.34 (±0.06)	97	0.00 ^{+0.05} _{-0.00}	1.29 ^{+0.14} _{-0.14}	1.9 ^{+0.10} _{-0.10}	1.5 ^{+0.10} _{-0.10}	7.02 ^{+1.49} _{-1.49}	-1.29 (±0.09)	0.804	-6.802
HIP 78092	6500 ⁺²⁵⁰ ₋₂₅₀	3.93 (±0.08)	140	0.00 ^{+0.05} _{-0.00}	0.90 ^{+0.12} _{-0.13}	1.6 ^{+0.10} _{-0.10}	2.2 ^{+0.10} _{-0.20}	8.08 ^{+1.94} _{-1.63}	-1.93 (±0.10)	0.158	-7.206
HIP 87819	9250 ⁺²⁵⁰ ₋₂₅₀	4.30 (±0.20)	101	0.00 ^{+0.05} _{-0.00}	1.23 ^{+0.23} _{-0.23}	1.9 ^{+0.10} _{-0.10}	1.6 ^{+0.00} _{-0.00}	7.56 ^{+2.17} _{-2.17}	-1.60 (±0.09)	0.486	-7.091
HIP 85755	10250 ⁺²⁵⁰ ₋₂₅₀	3.6 (±0.00)	142	0.00 ^{0.00} _{-0.00}	2.49 ^{+0.00} _{-0.00}	4.2 ^{+0.00} _{-0.00}	5.6 ^{+0.00} _{-0.00}	0.7 ^{+0.00} _{-0.00}	-1.23 (±0.00)	0.37	-7.000

Chapter 5

Conclusions

This thesis discussed the spectroscopic study of Herbig Ae/Be stars. The main objective was to determine the stellar parameters, accretion rates and IR excess of the stars. This chapter is a summary of the work in this thesis, along with the future prospects.

Herbig Ae/Be stars are Pre-Main Sequence stars having mass intermediate to that of T-Tauri stars and Massive Young Stellar Objects. These objects are ideal for studying as they are optically visible. To study the accretion rates and IR excess of these stars it is necessary to first determine the stellar parameters. In this work I determined the properties of a total of 18 stars using the spectra obtained using the XShooter instrument covering the wavelength range 3000-24800 Å, and measured their accretion rates and IR excesses.

Chapter 1 introduces topics like the star formation, Herbig stars and the protoplanetary disks around them, required to understand the thesis better. Chapter 2 discusses the sample selection and the homogeneous methods used to determine the stellar parameters. After their parameters were determined the stars were placed on the HR diagram and the young nature of the stars were confirmed and it was seen that the young stars in my sample tend to be more massive and hence are hotter.

Chapter 3 described how the accretion rates, \dot{M}_{acc} , were determined for the entire sample. It is an important information to understand how the Herbig stars evolve. The accretion rates obtained was plotted against the stellar parameters obtained in the previous chapter to understand how the stars evolve. It is seen that the accretion rates of young stars are higher than those of old stars, indicating that the accretion rates decreases as the stars approach the main sequence. The relationship between accretion rates and age is found to be $\dot{M}_{acc} \propto t^{-2.10 \pm 0.30}$, where t is the age, the relation between accretion rate and mass is found to be $\dot{M}_{acc} \propto M_*^{7.69 \pm 0.50}$ and that between the stellar luminosity and accretion luminosity is determined as $L_{acc} \propto L_*^{1.43 \pm 0.45}$. All these relations are found to be similar to that obtained in the previous works in literature, thus providing a broader set of sample to study about further. The IR excesses of the sample was determined and it was found that there is no clear trend between the IR excess and accretion rate in the sample in this work, but low accretors all have relatively lower IR excesses while there is a spread for high accretors. The lack of trend is not entirely unexpected because IR traces the dust and accretion traces the gas and the stars can have variable accretion rates with time.

In chapter 4, 4 stars which were already studied are included to the list of 18 stars which were studied in this work, to provide a broader understanding. Their parameters and accretion rates were also recorded. Later in this chapter, the values obtained in this work for Herbig stars were compared against those obtained in the previous work on Herbig stars. The relationship between the mass of the stars and the accretion rates for the overall sample (the sample from this work and the sample taken from Fairlamb et al. [2015]) is obtained as $\dot{M}_{acc} \propto M_*^{3.2 \pm 0.60}$ and that between the stellar luminosity and the accretion

luminosity is obtained as $L_{acc} \propto L_*^{1.25 \pm 0.10}$. These relations are found to be in agreement to that obtained in the previous works in literature.

Overall, the chapters in this thesis discussed:

- Determinations of the stellar parameters for the entire sample following a homogeneous fashion.
- Measurements of the accretion rates and IR excess. In addition, comparing the accretion rate with stellar parameters to see how they are related, and seeing how they vary for CTTs.
- Including the literature values and comparing the results of this work with that in the previous works.
- The conclusions that younger stars in this sample are seen to be massive and hence are hotter. Also, it is seen that young stars have higher accretion rates compared to the older ones, implying that the accretion rate decreases as the stars approach the main-sequence.
- The relationships between the accretion rates and stellar parameters obtained is found to be similar to that obtained in the literature.
- The IR excesses obtained showed that IR excess doesn't change with age indicating that dust is present at later ages also. Although, stars younger than 3 Myr are seen to have significant excesses. Also, high accretors have significant excesses indicating that when discs are young, the stars are young and they have high accretion rates and more excesses (in my sample stars as young as 3 Myr). Beyond 3 Myr there is no significant excess and also the accretion rates are low.

5.1 Future Prospects

Lately, many studies have been conducted on Herbig Ae/Be to understand how they function. Yet, there are many questions unanswered like how similar are they to CTTs and how they accrete. This thesis provides information to help create a better understanding of their accretion rates, how they vary with stellar parameters and they are related to the IR excess.

This work presents a study of an unbiased sample of pre-main sequence intermediate-mass stars, which is helpful to understand how these stars evolve. The IR excess emission measurements obtained in this work will be used in combination with the mid-IR excesses and stellar photosphere to characterise the inner disc and reveal inner hole sizes from the infrared Spectral Energy Distribution. Also, it would be valuable to systematically derive IR excesses for all stars having high accretion rates to get a clear view if the excesses are high when the accretion rates are high.

Bibliography

- B. Acke and M. E. van den Ancker. Resolving the disk rotation of HD 97048 and HD 100546 in the [O I] 6300 Å line: evidence for a giant planet orbiting HD 100546. , 449(1):267–279, Apr 2006. doi: 10.1051/0004-6361:20054330.
- B. Acke, M. E. van den Ancker, and C. P. Dullemond. [O I] 6300 Å emission in Herbig Ae/Be systems: Signature of Keplerian rotation. , 436:209–230, June 2005. doi: 10.1051/0004-6361:20042484.
- J. M. Alcalá, A. Natta, C. F. Manara, L. Spezzi, B. Stelzer, A. Frasca, K. Biazzo, E. Covino, S. Randich, and E. Rigliaco. X-shooter spectroscopy of young stellar objects. IV. Accretion in low-mass stars and substellar objects in Lupus. , 561:A2, Jan 2014. doi: 10.1051/0004-6361/201322254.
- E. Alecian, G. A. Wade, C. Catala, J. H. Grunhut, J. D. Landstreet, S. Bagnulo, T. Böhm, C. P. Folsom, S. Marsden, and I. Waite. A high-resolution spectropolarimetric survey of Herbig Ae/Be stars - I. Observations and measurements. , 429(2):1001–1026, Feb 2013. doi: 10.1093/mnras/sts383.
- R. Alexander, I. Pascucci, S. Andrews, P. Armitage, and L. Cieza. The Dispersal of Protoplanetary Disks. In Henrik Beuther, Ralf S. Klessen, Cornelis P. Dullemond, and Thomas Henning, editors, *Protostars and Planets VI*, page 475, Jan 2014. doi: 10.2458/azu_uapress_9780816531240 – ch021.
- P. André, J. Di Francesco, D. Ward-Thompson, S. I. Inutsuka, R. E. Pudritz, and J. E. Pineda. From Filamentary Networks to Dense Cores in Molecular Clouds: Toward a New Paradigm for Star Formation. In Henrik Beuther, Ralf S. Klessen, Cornelis P. Dullemond, and Thomas Henning, editors, *Protostars and Planets VI*, page 27, Jan 2014. doi: 10.2458/azu_uapress_9780816531240 – ch002.

- Ph. André, A. Men'shchikov, S. Bontemps, V. Könyves, F. Motte, N. Schneider, P. Didelon, V. Minier, P. Saraceno, and D. Ward-Thompson. From filamentary clouds to prestellar cores to the stellar IMF: Initial highlights from the Herschel Gould Belt Survey. , 518:L102, Jul 2010. doi: 10.1051/0004-6361/201014666.
- Philippe Andre, Derek Ward-Thompson, and Mary Barsony. Submillimeter Continuum Observations of rho Ophiuchi A: The Candidate Protostar VLA 1623 and Prestellar Clumps. , 406:122, Mar 1993. doi: 10.1086/172425.
- Sean M. Andrews, Katherine A. Rosenfeld, Adam L. Kraus, and David J. Wilner. The Mass Dependence between Protoplanetary Disks and their Stellar Hosts. , 771(2):129, Jul 2013. doi: 10.1088/0004-637X/771/2/129.
- Francesca Bacciotti, Thomas P. Ray, Reinhard Mundt, Jochen Eisloffel, and Josef Solf. Hubble Space Telescope/STIS Spectroscopy of the Optical Outflow from DG Tauri: Indications for Rotation in the Initial Jet Channel. , 576(1): 222–231, Sep 2002. doi: 10.1086/341725.
- T. Bagnoli, R. van Lieshout, L. B. F. M. Waters, G. van der Plas, B. Acke, H. van Winckel, G. Raskin, and P. D. Meerburg. An Inner Gaseous Disk Around the Herbig Be Star MWC 147. , 724:L5–L8, November 2010. doi: 10.1088/2041-8205/724/1/L5.
- Steven A. Balbus and John F. Hawley. A Powerful Local Shear Instability in Weakly Magnetized Disks. I. Linear Analysis. , 376:214, Jul 1991. doi: 10.1086/170270.
- A. Belloche. Observation of rotation in star forming regions: clouds, cores, disks, and jets. In P. Hennebelle and C. Charbonnel, editors, *EAS Publications Series*, volume 62 of *EAS Publications Series*, pages 25–66, Sep 2013. doi: 10.1051/eas/1362002.
- M. Benisty, A. Natta, A. Isella, J. P. Berger, F. Massi, J. B. Le Bouquin, A. Mérand, G. Duvert, S. Kraus, F. Malbet, J. Olofsson, S. Robbe-Dubois, L. Testi, M. Vannier, and G. Weigelt. Strong near-infrared emission in the sub-AU disk of the Herbig Ae star HD 163296: evidence of refractory dust? , 511:A74, Feb 2010. doi: 10.1051/0004-6361/200912898.
- T. Birnstiel, C. P. Dullemond, and F. Brauer. Gas- and dust evolution in protoplanetary disks. , 513:A79, Apr 2010. doi: 10.1051/0004-6361/200913731.

- Ralph C. Bohlin, Szabolcs Mészáros, Scott W. Fleming, Karl D. Gordon, Anton M. Koekemoer, and József Kovács. A New Stellar Atmosphere Grid and Comparisons with HST/STIS CALSPEC Flux Distributions. , 153(5):234, May 2017. doi: 10.3847/1538-3881/aa6ba9.
- S. Bontemps, P. Andre, S. Terebey, and S. Cabrit. Evolution of outflow activity around low-mass embedded young stellar objects. , 311:858–872, Jul 1996.
- J. Bouvier, S. H. P. Alencar, T. J. Harries, C. M. Johns-Krull, and M. M. Romanova. Magnetospheric Accretion in Classical T Tauri Stars. In Bo Reipurth, David Jewitt, and Klaus Keil, editors, *Protostars and Planets V*, page 479, Jan 2007.
- Alessandro Bressan, Paola Marigo, Léo. Girardi, Bernardo Salasnich, Claudia Dal Cero, Stefano Rubele, and Ambra Nanni. PARSEC: stellar tracks and isochrones with the PAdova and TRieste Stellar Evolution Code. , 427(1): 127–145, Nov 2012. doi: 10.1111/j.1365-2966.2012.21948.x.
- Sean D. Brittain, Joan R. Najita, John S. Carr, Joseph Liskowsky, Matthew R. Troutman, and Greg W. Doppmann. High-resolution Near-infrared Spectroscopy of HD 100546. II. Analysis of Variable Rovibrational CO Emission Lines. , 767(2):159, Apr 2013. doi: 10.1088/0004-637X/767/2/159.
- Nuria Calvet and Erik Gullbring. The Structure and Emission of the Accretion Shock in T Tauri Stars. , 509(2):802–818, Dec 1998. doi: 10.1086/306527.
- Nuria Calvet, James Muzerolle, César Briceño, Jesus Hernández, Lee Hartmann, José Luis Saucedo, and Karl D. Gordon. The Mass Accretion Rates of Intermediate-Mass T Tauri Stars. , 128(3):1294–1318, Sep 2004. doi: 10.1086/422733.
- A. Caratti o Garatti, R. Garcia Lopez, S. Antonucci, B. Nisini, T. Giannini, J. Eislöffel, T. P. Ray, D. Lorenzetti, and S. Cabrit. POISSON project. II. A multi-wavelength spectroscopic and photometric survey of young protostars in L 1641. , 538:A64, Feb 2012. doi: 10.1051/0004-6361/201117781.
- Jason A. Cardelli, Geoffrey C. Clayton, and John S. Mathis. The Relationship between Infrared, Optical, and Ultraviolet Extinction. , 345:245, Oct 1989. doi: 10.1086/167900.

- George R. Carruthers. Rocket Observation of Interstellar Molecular Hydrogen. , 161:L81, Aug 1970. doi: 10.1086/180575.
- C. Catala, E. Alecian, J. F. Donati, G. A. Wade, J. D. Landstreet, T. Böhm, J. C. Bouret, S. Bagnulo, C. Folsom, and J. Silvester. The magnetic field of the pre-main sequence Herbig Ae star HD 190073. , 462(1):293–301, Jan 2007. doi: 10.1051/0004-6361:20066264.
- P. Wilson Cauley and Christopher M. Johns-Krull. Optical Mass Flow Diagnostics in Herbig Ae/Be Stars. , 810(1):5, Sep 2015. doi: 10.1088/0004-637X/810/1/5.
- Paul Charbonneau and Keith B. MacGregor. Magnetic Fields in Massive Stars. I. Dynamo Models. , 559(2):1094–1107, Oct 2001. doi: 10.1086/322417.
- Roxana-Adela Chira. On Filaments within Molecular Clouds and their Connection to Star Formation. *arXiv e-prints*, art. arXiv:1806.02286, Jun 2018.
- L. M. Close, K. B. Follette, J. R. Males, A. Puglisi, M. Xompero, D. Apai, J. Najita, A. J. Weinberger, K. Morzinski, and T. J. Rodigas. Discovery of H α Emission from the Close Companion inside the Gap of Transitional Disk HD 142527. , 781(2):L30, Feb 2014. doi: 10.1088/2041-8205/781/2/L30.
- Thayne Currie, Takayuki Muto, Tomoyuki Kudo, Mitsuhiko Honda, Timothy D. Brandt, Carol Grady, Misato Fukagawa, Adam Burrows, Markus Janson, and Masayuki Kuzuhara. Recovery of the Candidate Protoplanet HD 100546 b with Gemini/NICI and Detection of Additional (Planet-induced?) Disk Structure at Small Separations. , 796(2):L30, Dec 2014. doi: 10.1088/2041-8205/796/2/L30.
- S. E. Dahm. A Spectroscopic Examination of Accretion Diagnostics for Near Solar Mass Stars in IC 348. , 136(2):521–547, Aug 2008. doi: 10.1088/0004-6256/136/2/521.
- D. de Winter, M. E. van den Ancker, A. Maira, P. S. Thé, H. R. E. Tjin A. Dije, I. Redondo, C. Eiroa, and F. J. Molster. A photometric catalogue of southern emission-line stars. , 380:609–614, Dec 2001. doi: 10.1051/0004-6361:20011476.

- Sarah E. Dodson-Robinson and Colette Salyk. Transitional Disks as Signposts of Young, Multiplanet Systems. , 738(2):131, Sep 2011. doi: 10.1088/0004-637X/738/2/131.
- C. Dominik, C. P. Dullemond, L. B. F. M. Waters, and A. Natta. *Models of Passive Disks with Inner Holes: Evidence for Disks around Intermediate Mass Pre-Main-Sequence Stars*, volume 287 of *Astronomical Society of the Pacific Conference Series*, pages 313–318. 2003.
- Brian Donehew and Sean Brittain. Measuring the Stellar Accretion Rates of Herbig Ae/Be Stars. , 141(2):46, Feb 2011. doi: 10.1088/0004-6256/141/2/46.
- C. P. Dullemond and C. Dominik. Dust coagulation in protoplanetary disks: A rapid depletion of small grains. , 434(3):971–986, May 2005. doi: 10.1051/0004-6361:20042080.
- C. P. Dullemond, C. Dominik, and A. Natta. Passive Irradiated Circumstellar Disks with an Inner Hole. , 560(2):957–969, Oct 2001. doi: 10.1086/323057.
- D. Egret, P. Didelon, B. J. McLean, J. L. Russell, and C. Turon. The TYCHO Input Catalogue. Cross- matching the Guide Star Catalog with the HIPPARCOS INCA Data Base. , 258:217–222, May 1992.
- Barbara Ercolano and Ilaria Pascucci. The dispersal of planet-forming discs: theory confronts observations. *Royal Society Open Science*, 4:170114, Apr 2017. doi: 10.1098/rsos.170114.
- J. Fairlamb. *A Spectroscopic Study Into Accretion In Herbig Ae/Be Stars*. PhD thesis, Ph. D. thesis, University of Leeds (2015), March 2015. URL <http://etheses.whiterose.ac.uk/id/eprint/9214>.
- J. R. Fairlamb, R. D. Oudmaijer, I. Mendigutía, J. D. Ilee, and M. E. van den Ancker. A spectroscopic survey of Herbig Ae/Be stars with X-shooter - I. Stellar parameters and accretion rates. , 453(1):976–1001, Oct 2015. doi: 10.1093/mnras/stv1576.
- J. R. Fairlamb, R. D. Oudmaijer, I. Mendigutia, J. D. Ilee, and M. E. van den Ancker. A spectroscopic survey of Herbig Ae/Be stars with X-Shooter - II. Accretion diagnostic lines. , 464(4):4721–4735, Feb 2017. doi: 10.1093/mnras/stw2643.

- D. Fedele, M. E. van den Ancker, Th. Henning, R. Jayawardhana, and J. M. Oliveira. Timescale of mass accretion in pre-main-sequence stars. , 510:A72, Feb 2010. doi: 10.1051/0004-6361/200912810.
- U. Finkenzeller and R. Mundt. The Herbig Ae/Be stars associated with nebulosity. , 55:109–141, Jan 1984.
- Gaia Collaboration. VizieR Online Data Catalog: Gaia DR2 (Gaia Collaboration, 2018). *VizieR Online Data Catalog*, art. I/345, Apr 2018.
- R. Garcia Lopez, A. Natta, L. Testi, and E. Habart. Accretion rates in Herbig Ae stars. , 459(3):837–842, Dec 2006. doi: 10.1051/0004-6361:20065575.
- L. M. Garrison, Jr. Observational studies of the Herbig Ae/Be stars. III - Spectrophotometry. , 224:535–545, September 1978. doi: 10.1086/156401.
- P. Ghosh and F. K. Lamb. Accretion by rotating magnetic neutron stars. II. Radial and vertical structure of the transition zone in disk accretion. , 232:259–276, Aug 1979. doi: 10.1086/157285.
- U. Gorti and D. Hollenbach. Photoevaporation of Circumstellar Disks By Far-Ultraviolet, Extreme-Ultraviolet and X-Ray Radiation from the Central Star. , 690(2):1539–1552, Jan 2009. doi: 10.1088/0004-637X/690/2/1539.
- U. Gorti, C. P. Dullemond, and D. Hollenbach. Time Evolution of Viscous Circumstellar Disks due to Photoevaporation by Far-Ultraviolet, Extreme-Ultraviolet, and X-ray Radiation from the Central Star. , 705:1237–1251, November 2009. doi: 10.1088/0004-637X/705/2/1237.
- A. J. Greenwood, I. Kamp, L. B. F. M. Waters, P. Woitke, and W. F. Thi. Effects of dust evolution on protoplanetary disks in the mid-infrared. , 626:A6, Jun 2019. doi: 10.1051/0004-6361/201834365.
- M. M. Guimarães, S. H. P. Alencar, W. J. B. Corradi, and S. L. A. Vieira. Stellar parameters and evidence of circumstellar activity for a sample of Herbig Ae/Be stars. , 457(2):581–589, Oct 2006. doi: 10.1051/0004-6361:20065005.
- Erik Gullbring, Lee Hartmann, Cesar Briceño, and Nuria Calvet. Disk Accretion Rates for T Tauri Stars. , 492(1):323–341, Jan 1998. doi: 10.1086/305032.

- Erik Gullbring, Nuria Calvet, James Muzerolle, and Lee Hartmann. The Structure and Emission of the Accretion Shock in T Tauri Stars. II. The Ultraviolet-Continuum Emission. , 544(2):927–932, Dec 2000. doi: 10.1086/317253.
- Lee Hartmann, Nuria Calvet, Erik Gullbring, and Paola D’Alessio. Accretion and the Evolution of T Tauri Disks. , 495(1):385–400, Mar 1998. doi: 10.1086/305277.
- G. H. Herbig. The Spectra of Be- and Ae-Type Stars Associated with Nebulosity. , 4:337, March 1960. doi: 10.1086/190050.
- Gregory J. Herczeg and Lynne A. Hillenbrand. UV Excess Measures of Accretion onto Young Very Low Mass Stars and Brown Dwarfs. , 681(1):594–625, Jul 2008. doi: 10.1086/586728.
- J. Hernández, N. Calvet, C. Briceño, L. Hartmann, and P. Berlind. Spectral Analysis and Classification of Herbig Ae/Be Stars. , 127:1682–1701, March 2004. doi: 10.1086/381908.
- Mark H. Heyer, John M. Carpenter, and Ronald L. Snell. The Equilibrium State of Molecular Regions in the Outer Galaxy. , 551(2):852–866, Apr 2001. doi: 10.1086/320218.
- David Hollenbach, Doug Johnstone, Susana Lizano, and Frank Shu. Photoevaporation of Disks around Massive Stars and Application to Ultracompact H II Regions. , 428:654, Jun 1994. doi: 10.1086/174276.
- S. Hubrig, B. Stelzer, M. Schöller, C. Grady, O. Schütz, M. A. Pogodin, M. Curé, K. Hamaguchi, and R. V. Yudin. Searching for a link between the magnetic nature and other observed properties of Herbig Ae/Be stars and stars with debris disks. , 502(1):283–301, Jul 2009. doi: 10.1051/0004-6361/200811533.
- A. Meredith Hughes, Gaspard Duchêne, and Brenda C. Matthews. Debris Disks: Structure, Composition, and Variability. , 56:541–591, Sep 2018. doi: 10.1146/annurev-astro-081817-052035.
- Laura Ingleby, Nuria Calvet, Gregory Herczeg, Alex Blaty, Frederick Walter, David Ardila, Richard Alexander, Suzan Edwards, Catherine Espaillat,

- and Scott G. Gregory. Accretion Rates for T Tauri Stars Using Nearly Simultaneous Ultraviolet and Optical Spectra. , 767(2):112, Apr 2013. doi: 10.1088/0004-637X/767/2/112.
- Andrea Isella, Antonella Natta, and Leonardo Testi. The Shape of the Inner Rim in Proto-Planetary Disks. In A. Richichi, F. Delplancke, F. Paresce, and A. Chelli, editors, *The Power of Optical/IR Interferometry: Recent Scientific Results and 2nd Generation*, page 515, Jan 2008. doi: 10.1007/978-3-540-74256-2_72.
- James M. Jackson, Susanna C. Finn, Edward T. Chambers, Jill M. Rathborne, and Robert Simon. The “Nessie” Nebula: Cluster Formation in a Filamentary Infrared Dark Cloud. , 719(2):L185–L189, Aug 2010. doi: 10.1088/2041-8205/719/2/L185.
- Silva P. Järvinen, Markus Schöller, Michail A. Pogodin, Andres Cahuasqui, Natalia A. Drake, S. Hubrig, Monika Petr-Gotzens, Igor S. Savanov, Ilya Ilyin, and Beate Stelzer. Spectroscopic Signatures Of Magnetospheric Accretion In Herbig Ae/Be Stars. In *19th Cambridge Workshop on Cool Stars, Stellar Systems, and the Sun (CS19)*, Cambridge Workshop on Cool Stars, Stellar Systems, and the Sun, page 74, Jul 2016. doi: 10.5281/zenodo.57995.
- Sarah M. R. Jeffreson and J. M. Diederik Kruijssen. A general theory for the lifetimes of giant molecular clouds under the influence of galactic dynamics. , 476(3):3688–3715, May 2018. doi: 10.1093/mnras/sty594.
- Christopher M. Johns-Krull. The Magnetic Fields of Classical T Tauri Stars. , 664(2):975–985, Aug 2007. doi: 10.1086/519017.
- S. J. Kenyon, M. Gómez, and B. A. Whitney. *Low Mass Star Formation in the Taurus-Auriga Clouds*, volume 4, page 405. 2008.
- Ralf S. Klessen, Fabian Heitsch, and Mordecai-Mark Mac Low. Gravitational Collapse in Turbulent Molecular Clouds. I. Gasdynamical Turbulence. , 535(2):887–906, Jun 2000. doi: 10.1086/308891.
- Arieh Koenigl. Disk Accretion onto Magnetic T Tauri Stars. , 370:L39, Mar 1991. doi: 10.1086/185972.

- S. Kraus, K. H. Hofmann, M. Benisty, J. P. Berger, O. Chesneau, A. Isella, F. Malbet, A. Meilland, N. Nardetto, A. Natta, T. Preibisch, D. Schertl, M. Smith, P. Stee, E. Tatulli, L. Testi, and G. Weigelt. The origin of hydrogen line emission for five Herbig Ae/Be stars spatially resolved by VLTI/AMBER spectro-interferometry. *A&A*, 489(3):1157–1173, Oct 2008. doi: 10.1051/0004-6361/200809946.
- Ryuichi Kurosawa, M. M. Romanova, and T. J. Harries. Multidimensional models of hydrogen and helium emission line profiles for classical T Tauri stars: method, tests and examples. *A&A*, 416(4):2623–2639, Oct 2011. doi: 10.1111/j.1365-2966.2011.19216.x.
- Min-Kai Lin. Dust settling against hydrodynamic turbulence in protoplanetary discs. *MNRAS*, 485(4):5221–5234, Jun 2019. doi: 10.1093/mnras/stz701.
- K.M. Maaskant, M. Honda, L. B. F. M. Waters, A. G. G. M. Tielens, C. Dominik, M. Min, A. Verhoeff, G. Meeus, and M. E. van den Ancker. Identifying gaps in flaring Herbig Ae/Be disks using spatially resolved mid-infrared imaging. Are all group I disks transitional? *A&A*, 555:A64, Jul 2013. doi: 10.1051/0004-6361/201321300.
- C. F. Manara, G. Rosotti, L. Testi, A. Natta, J. M. Alcalá, J. P. Williams, M. Ansdell, A. Miotello, N. van der Marel, M. Tazzari, J. Carpenter, G. Guidi, G. S. Mathews, I. Oliveira, T. Prusti, and E. F. van Dishoeck. Evidence for a correlation between mass accretion rates onto young stars and the mass of their protoplanetary disks. *A&A*, 591:L3, Jun 2016. doi: 10.1051/0004-6361/201628549.
- S. Marino, M. C. Wyatt, O. Panić, L. Matrà, G. M. Kennedy, A. Bonsor, Q. Kral, W. R. F. Dent, G. Duchene, and D. Wilner. ALMA observations of the η Corvi debris disc: inward scattering of CO-rich exocomets by a chain of 3-30 M_{\oplus} planets? *MNRAS*, 465(3):2595–2615, Mar 2017. doi: 10.1093/mnras/stw2867.
- Hirohiko Masunaga, Shoken M. Miyama, and Shu-ichiro Inutsuka. A Radiation Hydrodynamic Model for Protostellar Collapse. I. The First Collapse. *A&A*, 495(1):346–369, Mar 1998. doi: 10.1086/305281.
- G. Meeus, L. B. F. M. Waters, J. Bouwman, M. E. van den Ancker, C. Waelkens, and K. Malfait. ISO spectroscopy of circumstellar dust in 14 Herbig Ae/Be

- systems: Towards an understanding of dust processing. , 365:476–490, Jan 2001. doi: 10.1051/0004-6361:20000144.
- I. Mendigutía, N. Calvet, B. Montesinos, A. Mora, J. Muzerolle, C. Eiroa, R. D. Oudmaijer, and B. Merín. Accretion rates and accretion tracers of Herbig Ae/Be stars. , 535:A99, Nov 2011. doi: 10.1051/0004-6361/201117444.
- I. Mendigutía, A. Mora, B. Montesinos, C. Eiroa, G. Meeus, B. Merín, and R. D. Oudmaijer. Accretion-related properties of Herbig Ae/Be stars. Comparison with T Tauris. , 543:A59, July 2012. doi: 10.1051/0004-6361/201219110.
- I. Mendigutía, S. Brittain, C. Eiroa, G. Meeus, B. Montesinos, A. Mora, J. Muzerolle, R. D. Oudmaijer, and E. Rigliaco. Accretion Variability of Herbig Ae/Be Stars Observed by X-Shooter HD 31648 and HD 163296. , 776(1):44, Oct 2013. doi: 10.1088/0004-637X/776/1/44.
- S. Molinari, B. Swinyard, J. Bally, M. Barlow, J. P. Bernard, P. Martin, T. Moore, A. Noriega-Crespo, R. Plume, and L. Testi. Clouds, filaments, and protostars: The Herschel Hi-GAL Milky Way. , 518:L100, Jul 2010. doi: 10.1051/0004-6361/201014659.
- J. L. Monin, S. Guieu, C. Pinte, L. Rebull, P. Goldsmith, M. Fukagawa, F. Ménard, D. Padgett, K. Stappelfeld, C. McCabe, S. Carey, A. Noriega-Crespo, T. Brooke, T. Huard, S. Terebey, L. Hillenbrand, and M. Guedel. The large-scale disk fraction of brown dwarfs in the Taurus cloud as measured with Spitzer. , 515:A91, Jun 2010. doi: 10.1051/0004-6361/200912338.
- B. Montesinos, C. Eiroa, A. Mora, and B. Merín. Parameters of Herbig Ae/Be and Vega-type stars. , 495:901–917, March 2009. doi: 10.1051/0004-6361:200810623.
- A. Mora, B. Merín, E. Solano, B. Montesinos, D. de Winter, C. Eiroa, R. Ferlet, C. A. Grady, J. K. Davies, L. F. Miranda, R. D. Oudmaijer, J. Palacios, A. Quirrenbach, A. W. Harris, H. Rauer, A. Collier Cameron, H. J. Deeg, F. Garzón, A. Penny, J. Schneider, Y. Tsapras, and P. R. Wesselius. EXPORT: Spectral classification and projected rotational velocities of Vega-type and pre-main sequence stars. , 378:116–131, October 2001. doi: 10.1051/0004-6361:20011098.

- T. Ch. Mouschovias and E. V. Paleologou. The angular momentum problem and magnetic braking: an exact, time-dependent solution. , 230:204–222, May 1979. doi: 10.1086/157077.
- J. Muzerolle, L. Hartmann, and N. Calvet. Emission-Line Diagnostics of T Tauri Magnetospheric Accretion. I. Line Profile Observations. , 116:455–468, July 1998a. doi: 10.1086/300428.
- James Muzerolle, Nuria Calvet, and Lee Hartmann. Magnetospheric Accretion Models for the Hydrogen Emission Lines of T Tauri Stars. , 492(2):743–753, Jan 1998b. doi: 10.1086/305069.
- James Muzerolle, Nuria Calvet, and Lee Hartmann. Emission-Line Diagnostics of T Tauri Magnetospheric Accretion. II. Improved Model Tests and Insights into Accretion Physics. , 550(2):944–961, Apr 2001. doi: 10.1086/319779.
- James Muzerolle, Paola D’Alessio, Nuria Calvet, and Lee Hartmann. Magnetospheres and Disk Accretion in Herbig Ae/Be Stars. , 617(1):406–417, Dec 2004. doi: 10.1086/425260.
- James Muzerolle, Kevin L. Luhman, César Briceño, Lee Hartmann, and Nuria Calvet. Measuring Accretion in Young Substellar Objects: Approaching the Planetary Mass Regime. , 625(2):906–912, Jun 2005. doi: 10.1086/429483.
- Takenori Nakano. Magnetic braking of the rotation of molecular cloud cores. , 241:495–505, Dec 1989. doi: 10.1093/mnras/241.3.495.
- A. Natta, L. Testi, and S. Randich. Accretion in the ρ -Ophiuchi pre-main sequence stars. , 452(1):245–252, Jun 2006. doi: 10.1051/0004-6361:20054706.
- Richard P. Nelson and John C. B. Papaloizou. The interaction of giant planets with a disc with MHD turbulence - IV. Migration rates of embedded proto-planets. , 350(3):849–864, May 2004. doi: 10.1111/j.1365-2966.2004.07406.x.
- R. D. Oudmaijer, J. Palacios, C. Eiroa, J. K. Davies, D. de Winter, R. Fernet, F. Garzón, C. A. Grady, A. Collier Cameron, H. J. Deeg, A. W. Harris, K. Horne, B. Merín, L. F. Miranda, B. Montesinos, A. Mora, A. Penny, A. Quirrenbach, H. Rauer, J. Schneider, E. Solano, Y. Tsapras, and P. R. Wesselius. EXPORT: Optical photometry and polarimetry of Vega-type and

- pre-main sequence stars. , 379:564–578, Nov 2001. doi: 10.1051/0004-6361:20011331.
- R. D. Oudmaijer, K. M. Ababakr, and J. R. Fairlamb. The formation and evolution of Herbig Ae/Be stars . , 88:605, Jan 2017.
- F. Palla. *The Quest for Evolutionary Diagrams of Young Stellar Objects (Review)*, volume 465, page 143. 1996. doi: 10.1007/BFb0102632.
- F. Palla and S. W. Stahler. The formation and evolution of Herbig Ae/Be stars. In P. S. The, M. R. Perez, and E. P. J. van den Heuvel, editors, *The Nature and Evolutionary Status of Herbig Ae/Be Stars*, volume 62 of *Astronomical Society of the Pacific Conference Series*, page 391, 1994.
- O. Panic. *High angular resolution studies of protoplanetary discs*. PhD thesis, Ph. D. thesis, University of Leiden (2009), October 2009.
- O. Panić and M. Min. Effects of disc mid-plane evolution on CO snowline location. , 467(1):1175–1185, May 2017. doi: 10.1093/mnras/stx114.
- John C. B. Papaloizou, Richard P. Nelson, and Mark D. Snellgrove. The interaction of giant planets with a disc with MHD turbulence - III. Flow morphology and conditions for gap formation in local and global simulations. , 350(3): 829–848, May 2004. doi: 10.1111/j.1365-2966.2004.07566.x.
- I. Pascucci, L. Testi, G. J. Herczeg, F. Long, C. F. Manara, N. Hendler, G. D. Mulders, S. Krijt, F. Ciesla, Th. Henning, S. Mohanty, E. Drabek-Maunder, D. Apai, L. Szűcs, G. Sacco, and J. Olofsson. A Steeper than Linear Disk Mass-Stellar Mass Scaling Relation. , 831(2):125, Nov 2016. doi: 10.3847/0004-637X/831/2/125.
- N. Peretto, G. A. Fuller, A. Duarte-Cabral, A. Avison, P. Hennebelle, J. E. Pineda, Ph. André, S. Bontemps, F. Motte, and N. Schneider. Global collapse of molecular clouds as a formation mechanism for the most massive stars. , 555:A112, Jul 2013. doi: 10.1051/0004-6361/201321318.
- D. Polychroni, E. Schisano, D. Elia, A. Roy, S. Molinari, P. Martin, Ph. André, D. Turrini, K. L. J. Rygl, and J. Di Francesco. Two Mass Distributions in the L 1641 Molecular Clouds: The Herschel Connection of Dense Cores and Filaments in Orion A. , 777(2):L33, Nov 2013. doi: 10.1088/2041-8205/777/2/L33.

- L. Prato, T. P. Greene, and M. Simon. Astrophysics of Young Star Binaries. In *American Astronomical Society Meeting Abstracts*, volume 201, page 20.17, Dec 2002.
- J. E. Pringle. Accretion discs in astrophysics. , 19:137–162, Jan 1981. doi: 10.1146/annurev.aa.19.090181.001033.
- Sascha P. Quanz, Adam Amara, Michael R. Meyer, Matthew A. Kenworthy, Markus Kasper, and Julien H. Girard. A Young Protoplanet Candidate Embedded in the Circumstellar Disk of HD 100546. , 766(1):L1, Mar 2013. doi: 10.1088/2041-8205/766/1/L1.
- Andreas Quirrenbach, Sabine Reffert, Trifon Trifonov, Christoph Bergmann, and Christian Schwab. Planets around Giant Stars: Results from the Lick Survey. In *AAS/Division for Extreme Solar Systems Abstracts*, volume 47 of *AAS/Division for Extreme Solar Systems Abstracts*, page 502.01, Dec 2015.
- S. Reffert, C. Bergmann, A. Quirrenbach, T. Trifonov, and A. Künstler. Precise radial velocities of giant stars. VII. Occurrence rate of giant extrasolar planets as a function of mass and metallicity. , 574:A116, February 2015. doi: 10.1051/0004-6361/201322360.
- Sabine Reffert, Christoph Bergmann, Andreas Quirrenbach, Trifon Trifonov, and Andreas Künstler. Giant Planet Occurrence Rate as a Function of Stellar Mass. In *Protostars and Planets VI Posters*, Jul 2013.
- Á. Ribas, H. Bouy, and B. Merín. Protoplanetary disk lifetimes vs. stellar mass and possible implications for giant planet populations. , 576:A52, April 2015. doi: 10.1051/0004-6361/201424846.
- E. Rigliaco, A. Natta, L. Testi, S. Randich, J. M. Alcalà, E. Covino, and B. Stelzer. X-shooter spectroscopy of young stellar objects. I. Mass accretion rates of low-mass T Tauri stars in σ Orionis. , 548:A56, December 2012. doi: 10.1051/0004-6361/201219832.
- J. Rodmann, Th. Henning, C. J. Chandler, L. G. Mundy, and D. J. Wilner. Large dust particles in disks around T Tauri stars. , 446(1):211–221, Jan 2006. doi: 10.1051/0004-6361:20054038.

- S. Roessiger. Discussion of Infrared Measurements of T Tauri Stars and Related Objects. *Astronomische Nachrichten*, 298:215, Jan 1977. doi: 10.1002/asna.19772980405.
- S. I. Sadavoy, J. Di Francesco, Ph. André, S. Pezzuto, J. P. Bernard, A. Maury, A. Men'shchikov, F. Motte, Q. Nguyen-Lu'o'ng, and N. Schneider. Class 0 Protostars in the Perseus Molecular Cloud: A Correlation Between the Youngest Protostars and the Dense Gas Distribution. , 787(2):L18, Jun 2014. doi: 10.1088/2041-8205/787/2/L18.
- Sumanta Sahoo. *Episodic Accretion in V2493 Cyg*. PhD thesis, 07 2016.
- Anneila I. Sargent and Steven Beckwith. Kinematics of the Circumstellar Gas of HL Tauri and R Monocerotis. , 323:294, Dec 1987. doi: 10.1086/165827.
- B. Sato, H. Izumiura, E. Toyota, E. Kambe, M. Ikoma, M. Omiya, S. Masuda, Y. Takeda, D. Murata, Y. Itoh, H. Ando, M. Yoshida, E. Kokubo, and S. Ida. *Properties of Planets around G, K Giants*, volume 398 of *Astronomical Society of the Pacific Conference Series*, page 67. 2008.
- F. H. Shu. Self-similar collapse of isothermal spheres and star formation. , 214: 488–497, Jun 1977. doi: 10.1086/155274.
- Frank Shu, Joan Najita, Eve Ostriker, Frank Wilkin, Steven Ruden, and Susana Lizano. Magnetocentrifugally Driven Flows from Young Stars and Disks. I. A Generalized Model. , 429:781, Jul 1994. doi: 10.1086/174363.
- Aurora Sicilia-Aguilar, Thomas Henning, and Lee W. Hartmann. Accretion in Evolved and Transitional Disks in CEP OB2: Looking for the Origin of the Inner Holes. , 710(1):597–612, Feb 2010. doi: 10.1088/0004-637X/710/1/597.
- L. Siess, M. Forestini, and C. Dougados. Synthetic Hertzsprung-Russell diagrams of open clusters. , 324:556–565, Aug 1997.
- P. M. Solomon, N. Z. Scoville, and D. B. Sanders. Giant molecular clouds in the Galaxy: the distribution of ^{13}CO emission in the galactic plane. , 232: L89–L93, Sep 1979. doi: 10.1086/183042.
- P. M. Solomon, A. R. Rivolo, J. Barrett, and A. Yahil. Mass, Luminosity, and Line Width Relations of Galactic Molecular Clouds. , 319:730, Aug 1987. doi: 10.1086/165493.

- S. E. Strom, K. M. Strom, J. Yost, L. Carrasco, and G. Grasdalen. The Nature of the Herbig Ae- and Be-TYPE Stars Associated with Nebulosity. , 173:353, April 1972. doi: 10.1086/151425.
- P. S. The, D. de Winter, and M. R. Perez. A new catalogue of members and candidate members of the Herbig Ae/Be (HAEBE) stellar group. , 104:315–339, Apr 1994.
- I. Tilling, C. J. Clarke, J. E. Pringle, and C. A. Tout. Disc evolution and the relationship between L_{acc} and L_* in T Tauri stars. , 385(3):1530–1534, Apr 2008. doi: 10.1111/j.1365-2966.2008.12940.x.
- M. E. van den Ancker, J. Bouwman, P. R. Wesselius, L. B. F. M. Waters, S. M. Dougherty, and E. F. van Dishoeck. ISO spectroscopy of circumstellar dust in the Herbig Ae systems AB Aur and HD 163296. , 357:325–329, May 2000.
- G. van der Plas, M. E. van den Ancker, B. Acke, A. Carmona, C. Dominik, D. Fedele, and L. B. F. M. Waters. Evidence for CO depletion in the inner regions of gas-rich protoplanetary disks. , 500(3):1137–1141, Jun 2009. doi: 10.1051/0004-6361/200811148.
- G. van der Plas, M. E. van den Ancker, L. B. F. M. Waters, and C. Dominik. The structure of disks around Herbig Ae/Be stars as traced by CO ro-vibrational emission. , 574:A75, Feb 2015. doi: 10.1051/0004-6361/201425052.
- Schuyler van Dyk. Incremental Data Release from the Two Micron All Sky Survey (2MASS). *Be Star Newsletter*, 34:40, June 2000.
- F. van Leeuwen. Validation of the new Hipparcos reduction. , 474(2):653–664, Nov 2007. doi: 10.1051/0004-6361:20078357.
- J. Vernet, H. Dekker, S. D’Odorico, L. Kaper, P. Kjaergaard, F. Hammer, S. Randich, F. Zerbi, P. J. Groot, and J. Hjorth. X-shooter, the new wide band intermediate resolution spectrograph at the ESO Very Large Telescope. , 536:A105, Dec 2011. doi: 10.1051/0004-6361/201117752.
- S. L. A. Vieira, W. J. B. Corradi, S. H. P. Alencar, L. T. S. Mendes, C. A. O. Torres, G. R. Quast, M. M. Guimarães, and L. da Silva. Investigation of 131 Herbig Ae/Be Candidate Stars. , 126(6):2971–2987, Dec 2003. doi: 10.1086/379553.

- Jorick S. Vink, Janet E. Drew, Tim J. Harries, René D. Oudmaijer, and Yvonne Unruh. Probing the circumstellar structures of T Tauri stars and their relationship to those of Herbig stars. , 359(3):1049–1064, May 2005. doi: 10.1111/j.1365-2966.2005.08969.x.
- G. A. Wade, D. Drouin, S. Bagnulo, J. D. Land street, E. Mason, J. Silvester, E. Alecian, T. Böhm, J. C. Bouret, and C. Catala. Discovery of the pre-main sequence progenitors of the magnetic Ap/Bp stars? , 442(3):L31–L34, Nov 2005. doi: 10.1051/0004-6361:200500184.
- D. S. Wiebe. Chemical evolution of protoplanetary disks: the problem of initial conditions. In *A.A. Boyarchuk Memorial Conference*, pages 322–327, May 2018. doi: 10.26087/INASAN.2018.1.1.055.
- Jonathan P. Williams and Lucas A. Cieza. Protoplanetary Disks and Their Evolution. , 49(1):67–117, Sep 2011. doi: 10.1146/annurev-astro-081710-102548.
- N. Zacharias, D. G. Monet, S. E. Levine, S. E. Urban, R. Gaume, and G. L. Wycoff. The Naval Observatory Merged Astrometric Dataset (NOMAD). In *American Astronomical Society Meeting Abstracts*, volume 205, page 48.15, Dec 2004.